PCCP

Accepted Manuscript

ROYAL SOCIETY OF CHEMISTRY

www.rsc.org/pccp

Journal Name

RSCPublishing

ARTICLE

Charge Carrier Mobility in Organic Molecular Materials Probed by Electromagnetic Waves

Cite this: DOI: 10.1039/x0xx00000x

Shu Seki,* Akinori Saeki, Tsuneaki Sakurai and Daisuke Sakamaki

Received 00th January 2012,
Accepted 00th January 2012

DOI: 10.1039/x0xx00000x

www.rsc.org/

Charge carrier mobility is an essential parameter providing control over the performance of semiconductor devices fabricated using a variety of organic molecular materials. Recent design strategies toward molecular materials have been directed at the substitution of amorphous silicon-based semiconductors; accordingly, numerous measurement techniques have been designed and developed to probe the electronic conducting nature of organic materials bearing extremely wide structural variations in comparison with inorganic and/or metal-oxide semiconductor materials. The present perspective highlights the evaluation methodologies of charge carrier mobility in organic materials, as well as the merits and demerits of techniques examining the feasibility of organic molecules, crystals, and supramolecular assemblies in semiconductor applications. Beyond the simple substitution of amorphous silicon, we have attempted to address in this perspective the systematic use of measurement techniques for future development of organic molecular semiconductors.

1. Introduction

Growing concern with respect to the environmental compatibility of materials used in the field of electronics is leading to the enthusiastic pursuit of the discovery and development of conjugated organic molecules and their assemblies as candidates for organic semiconductor materials. Since demonstrating the considerable potential of organic molecules as electronic conductive materials,[1,2] their electronic properties have been progressively reported upon as represented by several benchmark reports on charge transfer complexes for organic electric conductors,[3] superconducting materials,[4] electronic conductive plastics,[5] the fabrication of devices such as transistors and light-emitting diodes, *etc*. In initial reports describing conductivity measurements of organic materials, copper phthalocyanine exhibited a considerably high conductivity of 10^{-1}–10^{-2} S cm^{-1} depending on temperature.[6] Current density, $J = \sigma E$, is given as the sum of electron (μ_e) and hole (μ_h) mobilities as follows:

Department of Applied Chemistry, Graduate School of Engineering, Osaka University, 2-1 Yamadaoka, Suita, Osaka 565-0871, Japan. E-mail: seki@chem.eng.osaka-u.ac.jp; fax: +81-6-6879-4586; tel.: +81-6-6879-4586

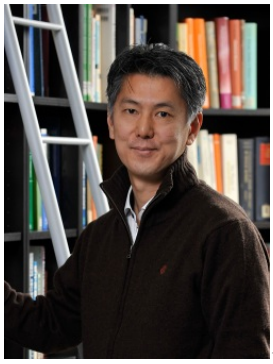

Shu Seki

Shu Seki graduated from the University of Tokyo in 1993, and received his PhD degree in 2001 from Osaka University. He joined Argonne National Laboratory, USA in 1993, and Delft University of Technology in 2001. He was appointed as Professor of Applied Chemistry, Graduate School of Engineering, Osaka University in 2009. His research is primarily focused on the physical chemistry of condensed matters, functional organic materials and nanomaterials.

Akinori Saeki

Akinori Saeki received his doctorate of engineering from Osaka University in 2007. He has worked as an Assistant Professor at Osaka University (2003–2009), a visiting researcher at Argonne National Laboratory (2002), and a JST-PRESTO researcher (2009). Currently, he is an Assistant Professor at Osaka University. His research interests include the fundamental understanding of short-lived chemical species in organic electronics, together with the development of evaluation methodologies and functional materials.

$$\sigma = en\mu_e + ep\mu_h, \quad (1)$$

where n and p are the density of mobile electrons and holes in the medium, respectively. The principal parameters determining the electric conductivity of materials are the values of mobility, μ_e and μ_h, which are assessed primarily by the measurement of the Hall effect (HE). Even in the case of copper phthalocyanine, the presumed value of μ_h reached up to 10 cm^2 V^{-1} s^{-1}, which was higher than the mobility of electrons and holes in amorphous silicon.[7,8] These pioneering works on organic semiconductor molecules suggested their high potential as candidates for semiconductor materials, substituting inorganic and oxide semiconductors; however, major practical applications of such materials have yet to be developed, even in the 21st century.

In contrast to the dramatic enhancement in electrical conductivity in organic materials as demonstrated by the ground-breaking work on perylene–halogen complexes,[9] TTF–TCNQ,[3] *etc.*—in some instances boosting the conductivity of the materials from 10^{-12} S cm^{-1} to 10^3 S cm^{-1}—the highest value of mobility has left in the same order until very recently. This may be due to the lower dynamic range of mobility measurement systems not only for organic but also inorganic and metal-oxide semiconductor materials. Starting with the HE measurement, a variety of methods have been developed to determine mobility values based on static and/or dynamic electromagnetics, which have been used for the assessment of organic semiconductor materials varying widely in chemical structures in comparison with those of inorganic and metal oxide semiconductor materials.

A breakthrough in charge carrier mobility was made by the expansion in dimensionality of flat or curled graphite materials, graphene, and carbon nanotubes.[10–12] Especially, the former displayed massless charge carriers (electrons) based on Dirac's band theory,[13] leading to extremely high mobilities up to 10^4–10^5 cm^2 V^{-1} s^{-1}. A practical target for charge carrier mobility in organic conductor/semiconductor development has been set in the range of $\mu > 10^3$ cm^2 V^{-1} s^{-1} for semiconductor devices using Si/Ge-based semiconductor materials, 1–100 cm^2 V^{-1} s^{-1} for amorphous silicon replacement, and 0.01–10 cm^2 V^{-1} s^{-1} for photovoltaic applications. Depending on the theoretical background of each application, each mobility measurement technique has been developed with its own dynamic ranges and sensitivities, which are suitable for the materials used; as such, the derived mobility values have rarely been comprehensively discussed with their respective parameters determining the motion of charge carriers. In the present perspective, we address the advantages and disadvantages of measurement techniques developed for mobility assessment in organic semiconductors, and describe comprehensive approaches to measuring the mobility and effective mass of charge carriers in organic materials.

2. Mobility measurement techniques

The HE measurement has been used for both organic and inorganic semiconductor materials toward the examination of charge carrier mobility of thermally induced charge carriers with sufficient dark current (with relatively low resistivity) under an applied electric field. The mobility of charge carriers can be estimated by the analysis of a magnetic field–induced Hall voltage observed in a conductor with a "static" electrical current. The "long-range translational" flow of charge carriers is induced by an external voltage applied to the specimen; thus, the HE measurement is one of the most reliable mobility measurement methodologies based on "static" and "long-range translational" movements of charge carriers in materials. With this in mind, we summarize briefly the principles of measurement techniques based on "static"/"dynamic" and "translational"/"local" motions.

Analysis of static, long-range translational motions

Schematic diagrams of measurements employing the Hall effect (HE), space-charge-limited current (SCLC), and field-effect transistor (FET) device are given in Fig. 1. The HE measurement remains the first choice for mobility assessment

Tsuneaki Sakurai

Tsuneaki Sakurai received his PhD degree in 2012 from the University of Tokyo, Japan, under the supervision of Prof. Dr. Takuzo Aida. He then worked as a postdoctoral research associate under Prof. Dr. Shu Seki at Osaka University, and from 2013, as a Research Fellow of the Japan Society for the Promotion of Science (JSPS). His research interests include development of functional soft materials based on π-electronic systems and measurements of their solid-state electronic properties.

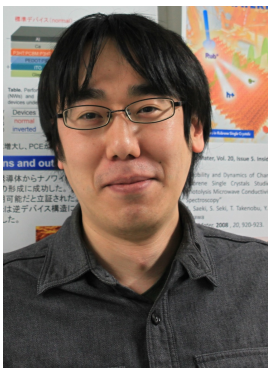

Daisuke Sakamaki

Daisuke Sakamaki received his Master's degree in 2010 and PhD degree in 2013 under the supervision of Prof. Dr. Kazuyoshi Tanaka from Kyoto University. He is currently working as a postdoctoral fellow of the Japan Society for the Promotion of Science (JSPS) in the group of Prof. Dr. Shu Seki at Osaka University. His research interests involve the synthesis and spectroscopic characterization of π-conjugated molecules and organic radicals.

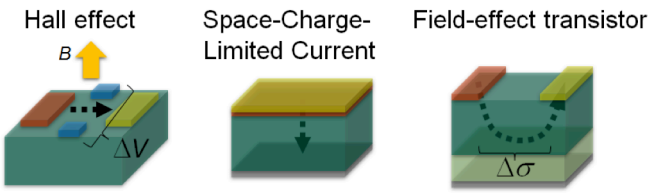

Fig. 1 Conceptual illustration of device structures used in direct current–based analysis techniques of charge carrier mobility: (left to right) Hall effect, space-charge-limited current, and field-effect transistor measurements.

of materials with a high enough conductivity using a static electrical current; the Hall coefficient (R_H) can be derived simply from the Hall voltage (V_H) trace in the medium without static current perturbation:[14]

$$V_H = R_H \frac{iB}{d}, \quad (2)$$

where B, i, and d are the magnetic field, total static current (= jdw, w is the width of the specimen), and thickness of the specimen, respectively. The Hall coefficient, R_H, can be expressed by the following expression with the terms μ_e and μ_h:

$$R_H = \frac{p\mu_h^2 - n\mu_e^2}{e\left(p\mu_h + n\mu_e\right)^2}. \quad (3)$$

Thus, quantitative analysis of the Hall coefficient with a modulated current density in the medium leads to the simultaneous determination of electron and hole drift mobilities as well as the charge carrier density. HE measurements are often carried out under a high magnetic field at low temperatures; the temperature dependence on R_H is used to assess the activation energy for the long-range translational motion of electrons or holes, as well as the Seebeck coefficient of the materials, which also allows the major charge carrier species to be assigned.

Organic conjugated molecules and their assemblies, however, are generally intrinsic semiconductor materials with relatively wide band gaps (E_g); thus, a small density of thermally activated charge carriers can be expected without any chemical dopants. The wide E_g of an organic semiconductor often leads to blocking contact for either electrons or holes, with Ohmic contacts for the counter charge carriers, because the work function of a metal electrode often takes the mid-value of E_g. In the case of electron injection through the Ohmic contact, the current density of the sandwich device consisting of a metal-(Ohmic)-semiconductor-(blocking)-metal structure is simply given by Ohm's law as

$$j = ne\mu_e E, \quad (4)$$

under a low electric field and negligibly small density of injected electrons in comparison with thermally activated carriers. However, with an increasing electric field, the density of electrons injected through the Ohmic contact promptly overcomes that of the thermally activated carriers, and the charge carriers dwell at the interface, resulting in space charges. The presence of space charges at the interface reduces the effective electric field at the interface and enhances the field in the semiconductor bulk, giving rise to SCLC. Based on the Child–Langmuir–Schottky equation for ballistic electron travelling without scattering,[15] the observed two-dimensional SCLC under an electric field E applied between parallel plate electrodes with an inter planar distance of d ($V = Ed$) can be given as

$$j = \frac{\sqrt{2}}{9\pi}\sqrt{\frac{e}{m}}\frac{V^{3/2}}{d^2}, \quad (5)$$

where m is the mass of the carriers. Practically, eqn (5) was developed to trace current under a lower electric field on the assumption of a constant carrier mobility μ in condensed matters, giving the Mott–Gurney law as follows:

$$j = \frac{9\varepsilon\varepsilon_0\mu V^2}{8d^3}, \quad (6)$$

Here, ε and ε_0 represent relative and absolute permittivity, respectively.[16] By analysis of static j under a varying electric field E, the value of mobility can be deduced directly as given in eqn (5); the charge carrier species (electron or hole) is also distinguished by the design of the Ohmic contacts of the SCLC device.

Static-current analysis by FET device response is the most widely used technique for assessment of organic semiconductor materials with a discretely defined value of mobility (μ_{FET}). As an analogue of the metal-oxide semiconductor (MOS)-FET deployed in silicon-based integrated electric circuits, an organic FET can evaluate charge carrier mobility parallel to the substrate. Charge carriers are injected from a source electrode and transported towards a drain electrode, while the corresponding current is modulated using a gate electrode voltage. Bottom-contact bottom-gate and top-contact bottom-gate configurations are often used, as an organic semiconducting layer can be easily deposited using a wet (*e.g.*, spin-coating and edge-casting) or dry process (*e.g.* thermal evaporation) on an insulating layer, which must be vigorously cleaned and carefully modified by self-assembled monolayer (SAM) formation. The charge carriers are presumed to reside on a very thin layer (one or two molecules thick) of the semiconducting layer, so that controlling energetic and morphological ordering at the interface between the insulator or SAM and semiconductor is of paramount importance to realize a high performance device.

Under an applied gate voltage (V_g), the source-drain current (I_d) is increased sublinearly with the source-drain voltage (V_d) and in an ideal case, is saturated at high V_d. This I_d–V_d curve is termed an output curve and leveled up with increasing V_g. When V_d is fixed in the saturation region, I_d increases superlinearly with V_g, showing a transfer curve characteristic as given by

$$|I_d| = \frac{WC}{2L}\mu_{FET}\left(V_g - V_{th}\right)^2, \qquad (7)$$

where W is the channel width, C is capacitance (= $\varepsilon_0\varepsilon_r/d$, ε_0: dielectric constant in vacuum, ε_r: relative dielectric constant, d: thickness of an insulator), L is the channel length, and V_{th} is the threshold voltage. The value of W should be much longer than L to suppress the contribution of curvature current. By fitting the experimental curve using eqn (7), both μ_{FET} and V_{th} can be evaluated. The ratio of maximum to minimum $|I_d|$ is the on–off ratio, reflecting the charge-transport property and the extent of dark current. It should be noted that FET can discern hole and electron mobilities by applying ($V_g < 0$ and $V_d < 0$) or ($V_g > 0$ and $V_d > 0$), respectively, where the source and drain electrodes need to be selected and fabricated in an appropriate manner.

Analysis of dynamic, long-range translational motions

Strategies used in HE and SCLC measurements have been well developed and verified by mobility determinations for a wide range of materials. However, these methodologies are applicable to conductors and semiconductors with enough high-charge carriers, and analysis is typically performed for the "static" electric current with relatively (in some case, extremely) high charge-carrier density; hence, analysis is performed under the interaction of charge carriers themselves. Analysis of electrical current also provides a statistical solution for charge carrier mobility, and the motion of charge carriers will not be traced directly by the measurements. Time-of-flight (TOF) measurements have often been chosen for mobility assessment in organic semiconductor materials, providing an explicit definition of "mobility". The plane-like charge carriers are produced by photo-ionization of materials or injection from a photocarrier-generating layer via laser-pulse irradiation, and the translational motions of charge carriers toward a counter electrode are promoted by the electric field applied to the sandwiched structure. The most important advantages of the TOF system are: 1) a direct trace of the dynamic motion of charge carriers, and 2) the flight time of charge carriers as the only requirement for mobility analysis. The latter secures the high experimental reliability of TOF in mobility assessments; however, it is essential that the geometry of the sandwich device with flat surfaces is fixed, and the fabricated materials are of high purity. The successful application of TOF measurement for mobility assessment has led to a variety of highly sophisticated formulations that are useful for the determination of not only mobility but also quantitative analysis of the drift-transporting mechanism and disorders/impurities present in the media. The initial expression for TOF mobility analysis is given by the Arrhenius activation mechanism as modified by Gill,[17]

$$\mu(T,E) = \mu_0 \exp\left(-\frac{\varepsilon_0 - \beta\sqrt{E}}{kT_{eff}}\right) \qquad (8),$$

$$1/T_{eff} = 1/T - 1/T_0$$

which represents the combined form of thermally activated hopping processes described by Arrhenius and the Poole–Frenkel law.[18] The organic bulk materials, however, often contain considerable amounts of impurities, disorders, and/or defects, which disturb the long-range translational motion even after careful purification of the materials. This leads to serious deformation of the transient photocurrent trace observed in the medium, and results in an inaccurate estimated mobility based on eqn (8). Taking into account the effects ascribed to the disordered structures, a disorder formalism was developed and successfully applied to the analysis of photocurrent traces.[19,20] Distributions in the energy levels of the hopping sites and spatial distribution of the sites were parameterized into σ_t and Σ_t, respectively, and the overall dependence of μ on E and T could be given by the following equation:[19]

$$\mu(T,E) = \mu_0 \exp\left[-\left(\frac{2\sigma_t}{3kT}\right)^2\right] \times \exp\left[C\left\{\left(\frac{\sigma_t}{kT}\right)^2 - \Sigma_t^2\right\}\sqrt{E}\right] \qquad (9)$$

This formulation provides a powerful method for analysis of the mechanisms of charge carrier transport with quantitative estimates of disordered structures in the media. As given in eqn (9), the actual values of mobility depend strongly on E and T, suggesting that the value of charge carrier mobility is not unique in case of dominance of the hopping transport in the media.

Analysis of dynamic, local motions

The highly sophisticated analysis required for determination of dynamic, long-range translational motion of charge carriers also suggests its sensitivity to trap-release processes, which are indispensable in promoting long-range translational motions of charge carriers with the unidirectional applied E; accordingly, the derived value of mobility is reflected strongly by the purity of materials.

The short-range oscillating motion of charge carriers has been often induced by the interaction between electromagnetic waves and charge carriers. In an intrinsic semiconductor material having a limited number of charge carriers with negligible conductivity of σ as in eqn (1), alternating electrical and magnetic fields are given by Maxwell's equations,

$$\Delta E = \frac{\partial}{\partial t}\left(\mu_m\varepsilon_m\frac{\partial^2}{\partial t^2}E + \mu_m\sigma E\right) \qquad (10)$$

$$\Delta B = \frac{\partial}{\partial t}\left(\mu_m\varepsilon_m\frac{\partial^2}{\partial t^2}B + \mu_m\sigma B\right), \qquad (11)$$

where μ_m and ε_m = $\varepsilon\varepsilon_0$ are magnetic permeability and permittivity, respectively. On the assumption of a sinusoidal function of the incident electromagnetic waves, the solution for eqn (10) and eqn (11) is given by

$$E(r,t) = E(r)\exp(i\omega t), \qquad (12)$$

and the electrical field of the waves is shown as

$$\Delta E(r) = \mu_m \left(i\sigma\omega - \varepsilon_m \omega^2 \right) E(r) \quad (13)$$

Thus, the complex dielectric constant of the medium with small electrical conductivity is given as

$$\varepsilon = \varepsilon_m - i\frac{\sigma}{\omega}, \quad (14)$$

and, by using ε, the Maxwell equation is expressed simply as

$$\Delta E(r) = \varepsilon \mu_m \omega^2 E(r) \quad (15)$$

This leads to a direct correlation with the complex dielectric constant and conductivity of the materials; the value of charge carrier mobility can be estimated quantitatively without using electrodes through an independent evaluation of n and p in eqn (1) by a precise analysis of the differential changes in the complex dielectric constant, which is attributed to the transient charge carriers injected into the materials. The derived value of mobility can be also discussed in terms of an effective mass of injected electrons or holes (m^*) as follows,

$$\mu = \frac{e\tau}{m^*}, \quad (16)$$

where τ is the relaxation time of charge carriers in translational motion. On the assumption of the time scale of the oscillating motion—hence the turn-over time of a probing electromagnetic wave being short enough relative to τ—eqn (16) directly gives an estimate of the effective mass of charge carriers.

Mobility measurement via the transient traces of complex dielectric constants with a small amount of injected charge carriers provides a great technical advantage as a non-contact, non-destructive screening process without the need for device fabrication. Unlike the above-described dynamic and static measurements, however, electrical amplification techniques are not applicable for the present measurement, because of its "non-contact" nature without an electrical current for amplification. Thus, the design of an electromagnetic wave cavity to promote interactions with the injected charge carriers plays a crucial role in the development of a highly sensitive system with wide dynamic range for mobility measurements.

With an electromagnetic wave cavity of a certain Q value (representing the microwave power loss in the cavity), the electromagnetic waves stored in the cavity interact with the transient charge carriers to continuously induce local oscillating motions (as much as ~Q times); this leads to an extremely high sensitivity to small changes in the complex dielectric constant of the sample loaded in the cavity (Fig. 2). Nevertheless the loss of electromagnetic waves in the cavity ($\Delta 1/Q$) cannot be measured directly by inserting probes, and the only observable value is the power (P_r) of microwaves reflected from the cavity and its transient changes (ΔP_r). The Q value can be further divided into Q_u, Q_c, and Q_s corresponding to the microwave interaction with the cavity inner walls, the coupling between the cavity and waveguide, and the sample, respectively.[21] The Q_u

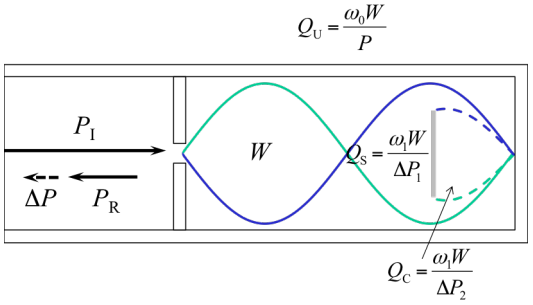

Fig. 2 Illustration of electromagnetic waves in the cavity with an unloaded Q value of Q_U.

and Q_c components remain constant during measurement of microwave power loss, so these can be included in Q_1. The relationship between Q_1, Q_s, and Q can be expressed as:

$$\frac{1}{Q} = \frac{1}{Q_1} + \frac{1}{Q_s} \quad (17)$$

The relationship between Q_s, ω_0, and the resonance frequency of the empty cavity, f_0 (= $\omega_0/2\pi$), is expressed by:[22]

$$\frac{\Delta\omega}{\omega_0} = \frac{\Delta f}{f_0} - i\Delta\left(\frac{1}{2Q_s}\right) \quad (18)$$

Electromagnetic waves passing through the sample give rise to a decrease in the electric field and a phase shift, as indicated by eqn (18), which causes a change in the Q value and resonant frequency. The intensity of the microwaves reflected from the cavity is expressed by eqn (19):

$$r = \left(\frac{\Delta\left(\frac{1}{Q_s}\right)\omega_0}{(\omega - \omega_0) - i\left(\frac{\omega_0}{2Q}\right)} + i \right) \quad (19)$$

The value of $\Delta P_r/P_r$ is defined by the complex conjugation of the reflectance:

$$r \cdot r^* = \frac{\Delta P_r}{P_r} = \frac{\left(\frac{\Delta\omega}{\omega_0}\right)^2 + \left(\frac{1}{2Q}\right)^2 + \frac{1}{Q}\Delta\left(\frac{1}{Q_s}\right) + \Delta\left(\frac{1}{Q_s}\right)^2}{\left(\frac{\Delta\omega}{\omega_0}\right)^2 + \left(\frac{1}{2Q}\right)^2}, \quad (20)$$

In the case of $\Delta\omega/\omega_0 \sim 0$, eqn (20) can be approximated by a linear function of $(1/Q_s)$,

$$\frac{\Delta P_r}{P_r} = \frac{\frac{1}{Q}\Delta\left(\frac{1}{Q_s}\right)}{\left(\frac{\Delta\omega}{\omega_0}\right)^2 + \left(\frac{1}{2Q}\right)^2} + \text{const} \quad (21)$$

Then, the dielectric loss of electromagnetic waves from the sample with mobile charge carriers in the cavity ($\Delta 1/Q_S$) is revealed to be proportional to $\Delta P_r/P_r$; hence, a non-contacting

and non-destructive measurement of conductivity can be achieved by the precise trace of the electromagnetic wave using dielectric spectroscopy.

Application of this spectroscopic technique to determine the conductivity of organic materials and mobility of charge carriers therein was developed by the pioneering work of Warman *et al.* at Delft University of Technology (Netherlands) using electromagnetic waves in the range of 10–50 GHz (microwaves).[23–25] This technique is referred to as pulse-radiolysis time-resolved microwave conductivity (PR-TRMC), as it generates transient charge carriers in the materials upon exposure to a pulsed high-energy electron beam. Because of the homogenous ionization of the primary component of the medium, the density of the generated charge carriers can be determined without performing other independent measurements, allowing a direct evaluation of charge carrier mobility from the accurate detection of dielectric loss. In contrast, the authors have focused on a flash-photolysis TRMC (FP-TRMC) utilizing exciton dissociation into charges as a charge-carrier injection scheme.[26–28] In the present FP-TRMC system, as expressed in eqn (21), kinetic traces of ΔP_r from a resonant cavity can be monitored after prompt photocarrier injection from a laser system with a time constant of ~10 ns, leading to the dynamic observation of charge carrier species as well as local motion.

One of the merits of the non-contact TRMC measurement is its applicability to a wide range of sample morphologies including powder, liquid, solution, film, crystallite forms, *etc*., leading to speedy and stable evaluation of the organic semiconductors without precise device fabrication and careful purification. In contrast, as given in eqn (1) and eqn (14), TRMC traces give only conductivity transients, where one cannot distinguish the contributions from the local motions of electrons and holes, respectively. It is also crucial to determine the density of injected charge carriers to deduce the values of mobility; to address these issues, the TRMC measurement has been often combined with transient absorption spectroscopy (TAS),[29–31] which assigns the conductive chemical transients quantitatively using n and p in eqn (1) as a function of time.

Analysis of static, local motions

Another approach to quantitative evaluation of n and p in the TRMC measurement is the field-induced injection of charge carriers through metal electrodes. Recently, a novel electromagnetic wave–based measurement was developed comprising field-induced TRMC (FI-TRMC) for evaluating charge carrier mobility at the interface between insulators and semiconductors without grain boundary effects.[32] A schematic diagram of the FI-TRMC measurement system is displayed in Fig. 3 with a typical microwave conductivity transient in accordance with the transient current monitored by an external circuit. From the viewpoint of practical applications of organic semiconducting materials, the static conductive channels of electrons or holes are always located at the interfaces of

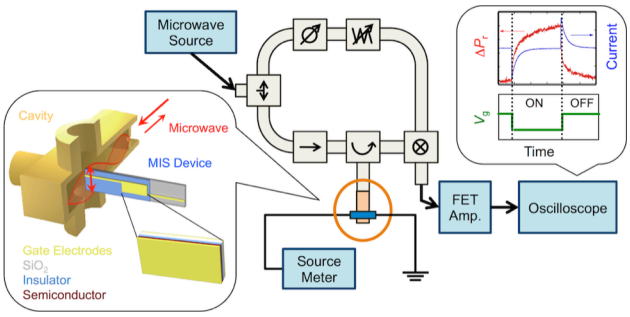

Fig. 3 Schematic diagram of FI-TRMC measurement system. The MIS device is loaded into the microwave cavity, and the transient current injected into the device is monitored independently by an external electric circuit, giving a reasonable estimate of charge carriers accumulated at semiconductor–insulator interface.

semiconductor–insulator, semiconductor–semiconductor, and/or semiconductor–metal materials. Although metal–insulator–semiconductor (MIS) device fabrication is indispensable in spectroscopic analysis, this FI-TRMC measurement system involves charge-carrier accumulation at insulator–semiconductor interfaces by applying a gate bias and evaluation of carrier mobilities through non-contact microwave probing, which potentially clarifies the local motion and dynamics of charge carriers at any interfacial structures found in practical devices such as FETs, organic light-emitting diodes (OLEDs), organic photovoltaics (OPVs), *etc*.

Electromagnetic wave interaction with mobile charge carriers in the cavity has also been discussed in terms of electron spin resonance (ESR) spectroscopy. As demonstrated in FI-TRMC measurements, MIS and FET devices have been successfully loaded into the microwave cavity, allowing for real-time monitoring of the direct current–based mobility of charge carriers by the external electrical circuit. Simultaneously, under a magnetic field, the paramagnetic nature of charge carriers (radical cations (holes) and anions (electrons)) permits measurement of their mobility by ESR spectroscopy via Zeeman splitting, which leads to the quantitative analysis of the number of spins and electronic states of the excess electrons. The line width (ΔH) of the ESR spectrum, which is ascribed to the injected charge carrier species, is proportional to the number of nuclear spins (n_n) in correlation with the carriers based on the random walk model as follows:[33]

$$\Delta H \propto A_n \left(n_n\right)^{1/2}, \qquad (22)$$

where A_n is the hyperfine coupling constant of the nuclear spins. Eqn (22) gives the degree of charge-carrier migration as a signature in the ESR spectrum, and an empirical relationship between FET mobility and n allows us to estimate the presumed value of mobility in the medium by simple FI-ESR spectroscopy.

In the remainder of this perspective, we will highlight the recent representative outcomes of our research, in particular

for organic crystalline materials (Section 3) and small-molecules-based soft materials (Section 4), especially those featuring the mobility evaluations by means of FP-TRMC and TAS techniques. Finally, recent applications of ESR spectroscopy addressing charge-carrier transport phenomena will be discussed separately in Section 5.

3. Charge carrier mobility in π-conjugated molecular crystals

Semiconducting π-conjugated molecules are a pervasive class of materials that show promise in providing flexible and bio-compatible organic field-effect transistors (OFETs), which can be manufactured by low-cost printing technologies.[34–37] Charge carrier mobility, one of the most important parameters of OFET devices, is susceptible to the complicated interplay between molecular packing, morphology, disorder, impurities, and interface characteristics. When considering hole (electron) transfer reactions among two identical molecules, its transfer rate (k) is formulated by the Marcus theory, incorporating charge transfer integral (ΔV) and reorganization energy (λ) as follows:[38]

$$k = \frac{4\pi^2}{h}\Delta V^2 \frac{1}{\sqrt{4\pi k_B \lambda T}} e^{\left(-\frac{\lambda}{4k_B T}\right)}, \qquad (23)$$

where h, k_B, and T are the Planck constant, Boltzmann constant, and absolute temperature, respectively. The values of ΔV and λ are characterized by the overlap of adjacent molecular orbitals involved in the charge transport and relaxation energy of charged and neutral species in their respective atomic coordinates, respectively. Maximizing ΔV and minimizing λ lead to an increase in charge carrier mobility; thus, the use of large and rigid π-planes such as acenes, heteroacenes, and discotic arenes is a rational strategy to this end. Furthermore, molecular orientation and distance are intimately associated with ΔV, which is controlled by engineering various interactions such as π–π, CH–π, hydrogen bonding, hydrophilic, and hydrophobic.

Pentacene is an acene composed of five fused benzenes (Fig. 4), which exhibits small λ, thermal evaporation without decomposition, and environmental stability. Although the poor resistance of pentacene to oxidation hinders its practical use, it has served as a pilot scaffold in OFET devices, not only for optimizing and understating the charge transport property, but also facilitating the fabrication of solution-processable TIPS-pentacene,[39] *n*-type perfluoropentacene,[40] and π-extended hexacene.[41] The hole mobility of pentacene thin film has seen an impressive advance from 0.1 $cm^2\ V^{-1}\ s^{-1}$ at the early stages[42–44] to 3–6 $cm^2\ V^{-1}\ s^{-1}$ via film processes and gate insulator modifications,[45–47] which has had great impact on improved herringbone-packing ordering and tailoring of fine-grain features. The highest mobility of pentacene has reached the value predicted by the Marcus theory,[48] demonstrating the remarkable experimental progress of OFETs in the past decade.

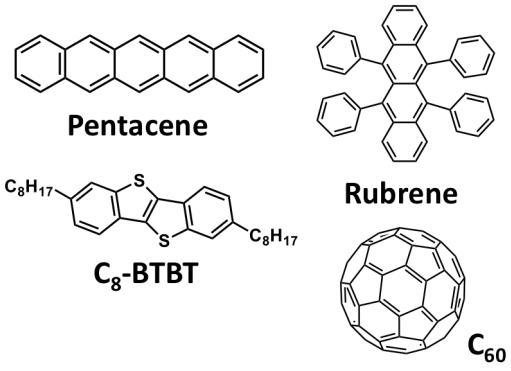

Fig. 4 Chemical structures of representative π-conjugated semiconducting molecules.

In spite of the important electric properties of pentacene, it is not readily amenable to evaluation of its photo-induced conductivity. Therefore, we have only reported an FP-TRMC charge carrier mobility of 0.7 $cm^2\ V^{-1}\ s^{-1}$ as the minimum intra-grain value, using a high-energy photon source capable of direct ionization.[49] Recently, our novel FI-TRMC technique revealed a hole mobility of 6.3 $cm^2\ V^{-1}\ s^{-1}$,[32] matching the highest FET value and corroborating that TRMC mobility is relevant to charge transfer among adjacent molecules in crystalline molecular semiconductors.

Other good examples of the correlation between Marcus theory and TRMC studies are self-organized semiconducting materials such as liquid crystals, nanotubes, nanowires, and gels. The next section is directed towards overviewing TRMC studies on these cutting-edge motifs. Compared with molecular crystals, self-organized materials have a wider distribution of molecular arrangement in terms of π–π distance, orientation, and energetic landscape, owing to their "soft" natures.[50] Gemini-shaped hexa-*peri*-hexabenzocoronene (HBC) amphiphiles developed by Fukushima and Aida *et al.* have demonstrated self-assembly to form a coaxial nanotubular structure consisting of a π-stacked HBC core (Fig. 5a and b).[51] Wide-angle X-ray diffractions (WAXD) using synchrotron radiation clarified the precise conformation of HBC stacking in the nanotube[52] and allowed us to calculate hole mobility based on the Marcus theory using the Amsterdam density functional (ADF) program[53] and reported methods.[54,55] The obtained value was 4.8 $cm^2\ V^{-1}\ s^{-1}$ at room temperature (ΔV = 115 meV and λ = 87 meV), which is almost equivalent to the FP-TRMC mobility of 2–3 $cm^2\ V^{-1}\ s^{-1}$ (Fig. 5c).[56,57] In contrast, a long-range mobility estimated by OFET characterization[56] or analysis of charge recombination of FP-TRMC kinetics[57] was on the order of 10^{-4} $cm^2\ V^{-1}\ s^{-1}$. This large gap is rationalized by the incorporation of two charge-transport processes: intra-tubular and inter-tubular hopping. The former is likely dominated by ΔV and λ of the HBC molecules, while the latter is considerably affected by tubular outer-shell morphology. Another noteworthy finding is that the mobilities in these two processes are in a trade-off relationship; therefore, it is essential

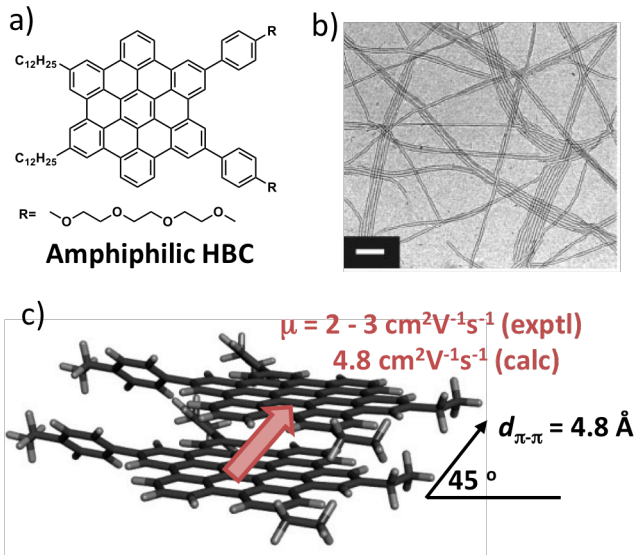

Fig. 5 (a) Chemical structure of Gemini-shaped HBC. b) TEM image of HBC nanotube. The scale bar indicates 200 nm. Reproduced with permission from ref. 51. Copyright 2004 AAAS. (c) Comparison between experimental mobility obtained by FP-TRMC (exptl) and that calculated by Marcus theory (calc).

to improve the electrical connectivity among nanotubes without disrupting their pronounced local charge transport. Technological improvements in this regard might include post-modification to separate the formation processes of nanostructure and smooth film, macroscopic alignment, and dimensional control.

It should be mentioned that quantum effect associated with the intramolecular reorganization energy leads to the modification of semi-classical Marcus given by eqn (23). The Marcus-Levich-Jortner (MLJ) formalism is cast in the following form.[58,59]

$$k = \frac{4\pi^2}{h}\Delta V^2 \frac{1}{\sqrt{4\pi k_B \lambda_{class} T}} \sum_{n=0}^{\infty}\left[\frac{S_{eff}^n}{n!} e^{-S_{eff}} \exp\left(-\frac{(\lambda_{class} + n\hbar\omega_{eff})^2}{4k_B\lambda_{class}T}\right)\right], \quad (24)$$

where λ_{class} is the classical contribution to the reorganization energy, S_{eff} is the Huang-Rhys (HR) factor,[59,60] ω_{eff} is the single effective mode of frequency, and $\hbar$ is the reduced Planck constant ($\hbar = h/2\pi$). The S_{eff} and ω_{eff} are associated with the quantum description of the nonclassical degrees of freedom. Negri *et al.* have applied the MLJ theorem to the perylene bisimides[61,62] and organic crystals,[63] and they found a delicate interplay of intra and intermolecular contributions to the charge carrier propagation. The MLJ framework is important when $\hbar\omega$ is much larger than the thermal energy k_BT,[59] suggesting that controlling the intramolecular vibrational mode has a critical impact on the modulation of charge transport process. Troisi has pointed out that the hopping model is valid only when ΔV is smaller than the half of λ.[64] Since ΔV of hole in pentacene and HBC nanotube are almost comparable to the respective λ, the simple hopping model of Marcus and MLJ models might be not appropriate for describing the charge transport between the neighboring two molecules. Nonetheless, macroscopic charge transport is still often governed by the hopping process between trapping sites as formulated by eqn (9).

A single crystal of a π-conjugated molecule is a superior substrate for comprehensive study of its electrical properties, as the trap density originating from structural defects and hopping barriers among the grains are minimized, allowing direct evaluation of the intrinsic charge carrier mobility. Surprisingly, pentacene in its single crystalline form has demonstrated hole mobility as high as 35 $cm^2\ V^{-1}\ s^{-1}$,[65] far exceeding the Marcus hopping rate and mobility in inorganic amorphous silicon. Currently, the highest mobility of 43 $cm^2\ V^{-1}\ s^{-1}$ was achieved in a rubrene single crystal OFET prepared by physical vapor deposition[66] (typical values range from 2 to 20 $cm^2\ V^{-1}\ s^{-1}$).[67–70] Despite the excellent transport properties of a π-conjugated single crystal, practical issues still remain; namely, precise control of patterning and rapid fabrication over a large substrate area. To overcome this drawback, state-of-the-art technologies such as blade casting, micro contact printing, and inkjet printing have evolved as versatile methods for solution-processed single-crystal OFETs. Notably, Takeya *et al.* reported a high hole mobility of 5 $cm^2\ V^{-1}\ s^{-1}$ for alkyl end-capped heteroacene, 2,7-dioctyl[1]benzothieno[3,2-*b*][1]benzothiophene (C_8-BTBT, Fig. 4).[71] Hasegawa *et al.* have developed an inkjet printing technique incorporating antisolvent droplet-triggered crystallization and have demonstrated an impressive hole mobility of 31.3 $cm^2\ V^{-1}\ s^{-1}$ for C_8-BTBT.[72] Bao *et al.* have utilized a droplet-pinned crystallization method to produce aligned single-crystalline ribbons of fullerene (C_{60}) over a large area, demonstrating a high electron mobility of 11 $cm^2\ V^{-1}\ s^{-1}$.[73] These values are, indeed, comparable or even higher than those of single crystals. As for FP-TRMC measurements, a crystal of an adamantylidene derivative of La@C_{82} showed an electron mobility over 10 $cm^2\ V^{-1}\ s^{-1}$,[74–76] in good accordance with the crystalline C_{60} ribbon. On the other hand, the sum of charge carrier mobilities in single-crystal rubrene was 0.052 $cm^2\ V^{-1}\ s^{-1}$ (70% hole and 30% electron),[77] much smaller than OFET results. The discrepancy was discussed from the viewpoints of frequency dependence, charge carrier density, *etc.*, and is still under debate. Regarding the observed exceptionally high OFET mobility, Takeya *et al.* have performed investigations on the Hall effect in a rubrene single crystal and elucidated that hole transport follows the band conduction mechanism rather than hopping, suggesting that the positive charge is delocalized on multiple neighbouring molecules.[78]

Distinct anisotropic mobility along the respective axis is another characteristic intrinsic to single crystals. The microwave electric field in a resonant cavity is fixed, and thus, one can readily evaluate anisotropic TRMC mobility with high angle resolution simply by rotating a crystal. A rubrene single crystal showed an anisotropy of 2.3 (Fig. 6a),[77] in line with the values of 2–3 as assessed by OFET.[67,68,79] Furthermore, FP-TRMC is applicable to needle-like crystals and fibers, which are difficult to access by conventional OFET configurations,

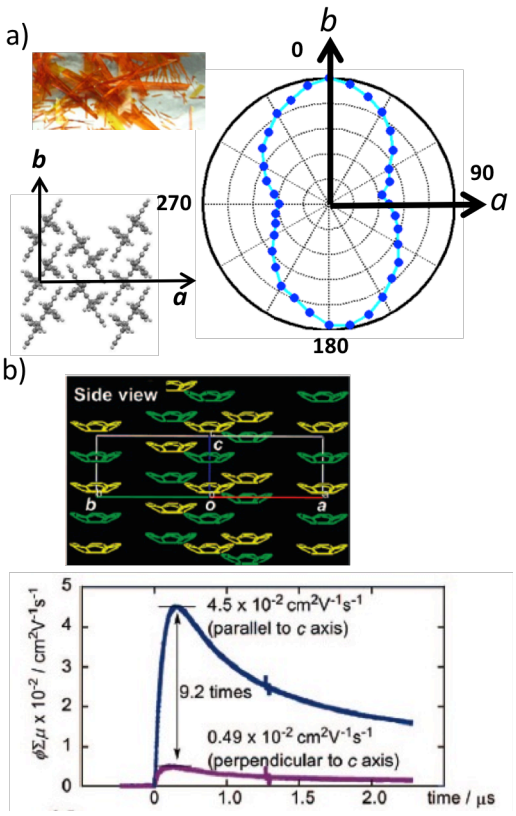

Fig. 6 (a) Anisotropy measurement of rubrene single crystal by FP-TRMC. The picture of crystals and crystalline structure are appended. Reproduced with permission from ref. 77. Copyright 2008 Wiley-VCH Verlag GmbH & Co. KGaA. (b) Anisotropy measurement of sumanene needle crystal by FP-TRMC. Reproduced with permission from ref. 80. Copyright 2009 American Chemical Society.

e.g., 9.2 for a sumanene needle crystal (Fig. 6b)[80], 10 for a self-assembled HBC nanotube.[81] The correlation between photoconductivity and amplified spontaneous emission (ASE) is also an important feature toward exploiting the intriguing optical features of single crystals,[82] *e.g.* lasing and light-emitting devices. Feasibility of unprocessible crystalline organic semiconductor materials can be also screened by the non-contact technique, revealing recently the electric conducting nature of metal-organic-framework systems[83,84], 3D π-conjugated molecules,[85–87] *etc*.

Together with the outstanding mobility and advances in large area processing, π-conjugated molecular crystals have occupied a notable posit ion in both practical application and fundamental investigation of structure–property relationships. For instance, crystalline domains in polymer–fullerene photovoltaics play a key role in the formation of hierarchical structures,[88] ensuring efficient charge separation and transport.[89]

4. Charge carrier mobility in supramolecular soft materials

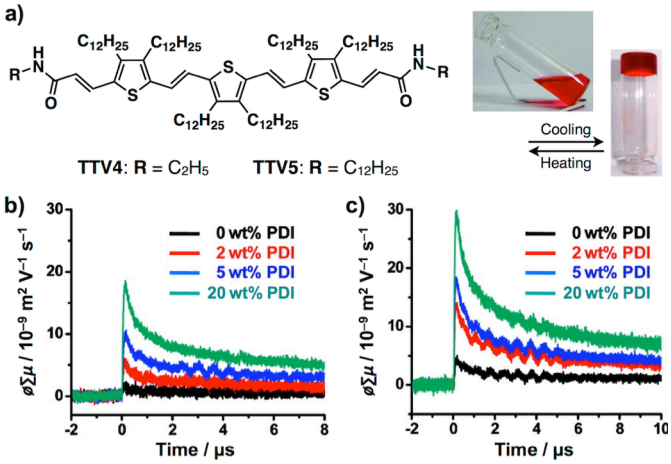

Fig. 7 (a) Molecular structures of **TTV4** and **TTV5**. Photographs of **TTV4** gel in decane during heating and cooling. FP-TRMC transient conductivity profiles (λ_{ex} = 355 nm) of **TTV4/PDI** films prepared from (b) $CHCl_3$ and (c) decane/$CHCl_3$ (1:1 v/v) solutions. The color represents weight fraction of PDI relative to 100 wt% **TTV4**. Reproduced with permission from ref. 100. Copyright 2010 American Chemical Society.

π-Conjugated molecules capable of self-assembly via supramolecular interactions are promising materials for the development of semiconducting nano-sized objects that transport charge carriers unidirectionally over long distances.[90–93] By taking advantage of the non-contact electrodeless method, we can evaluate the charge carrier transport properties for such supramolecular materials by using drop-cast or spin-coated samples. In this section, we summarize recent reports of self-assembling features and TRMC-based mobility evaluations about supramolecular soft materials, including nanofibers, nanotubes, insulated molecular wires, and liquid crystals.

Nanofibers

Nanofibers, as one of the most typical supramolecular materials, are formed through the solvent-assisted nanofibrous assembly of π-conjugated molecules. Several pioneering examples of such electroactive nanowires were reported nearly a decade and a half ago, many of which used π-conjugated aromatic motifs combined with hydrogen-bonding units. For instance, mono- and bithiophene derivatives with urea functionalities are known to self-assemble into nanofibers, which display highly mobile charge carriers in PR-TRMC.[94] Longer linear π-conjugated systems such as oligothiophene and oligo(*p*-phenylenevinylene) carrying hydrogen-bonding units self-assemble into nanofibers and further form organogels in a certain type of solvent.[95–99] In a recent typical example, Ajayaghosh *et al.* reported thienylenevinylene-based gelators that form organogels in nonpolar solvents (Fig. 7).[100,101] While a solution of **TTV4** in $CHCl_3$ (1.5×10^{-4} M) showed a π–π* absorption maximum at 501 nm, its λ_{max} was blue-shifted to 464 nm with a shoulder band at 550 nm in decane, indicating a strong exciton coupling due to the *H*-type aggregation of the constituent thienylenevinylenes. A drop-cast film of **TTV4** from decane/$CHCl_3$ (1:1 v/v) showed transient conductivity upon

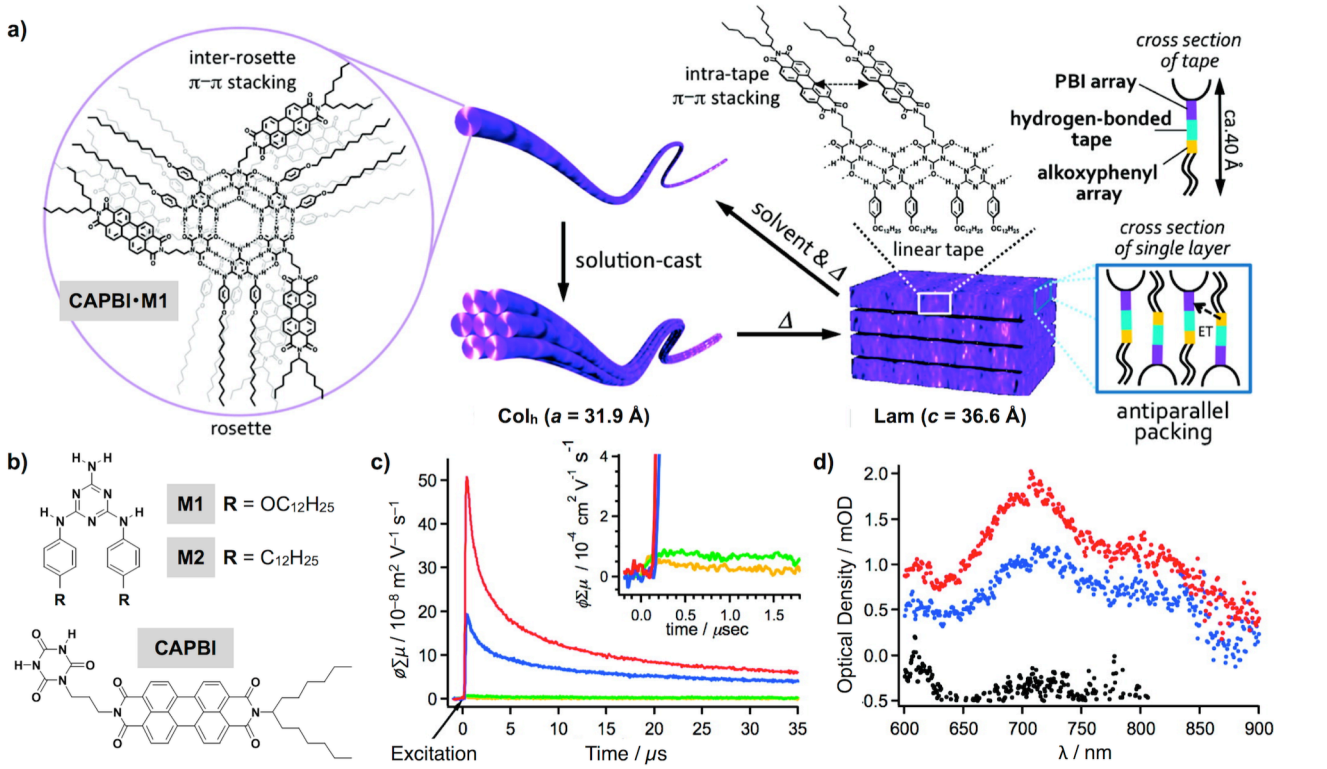

Fig. 8 (a) Schematic illustrations of the thermoresponsive supramolecular organization of **CAPBI·M1**. (b) Molecular structures of **M1**, **M2**, and **CAPBI**. (c) Conductivity transients of thin films of **CAPBI** (green), **M1** (orange), and **CAPBI·M1** in the Col_h (blue) and Lam structures (red) upon excitation with a 355 nm laser pulse (photon density = 1.4×10^{16} photons cm^{-2}). Inset shows a magnification of the graph. (d) TAS of **CAPBI·M1** in the Col_h (blue) and Lam structures (red) and of **CAPBI·M2** in the Lam structure (black) observed at 2 μs after photoexcitation (photon density = 1.8×10^{16} photons cm^{-2}). Reproduced with permission from ref. 105. Copyright 2010 American Chemical Society.

photoirradiation, exhibiting a maximum value larger than that from $CHCl_3$ solution. Furthermore, when a typical electron-accepting species, *N,N′*-bis(2,5-di-tert-butylphenyl)-3,4,9,10-perylenedicarboximide (**PDI**), was added into **TTV4** solution, its cast film exhibited much larger conductivity ($\varphi\sum\mu$) depending on the doped **PDI** contents (Fig. 7b and c), which is attributed to the photo-induced charge separation between donor and acceptor to afford increased φ values. From the characteristic transient absorption of **PDI** radical anion, the mobility value ($\sum\mu$) for **TTV4** was evaluated as ~1.5×10^{-2} and 6.0×10^{-2} cm^2 V^{-1} s^{-1} for the films from $CHCl_3$ and decane/$CHCl_3$, respectively. The above results strongly demonstrate the importance of the fibrous assembly on charge carrier mobility and the utility of fibrous morphology in donor–acceptor mixtures.

More complex dye assembly[102–104] is worthy of investigation to clarify the relationship between supramolecular structures and charge-carrier transport properties. Yagai *et al.* reported the formation of a multiple hydrogen bonding–mediated "rosette" and linear assembly using perylenebisimide and melamine-based molecules (Fig. 8).[105] PBI-appended cyanuric acid (**CAPBI**) self-assembled into a rosette-type macrocycle when complexed with **M1** or **M2** in 1:1 stoichiometry, which was followed by the formation of nanofibers via π-stacking of PBI moieties. X-ray diffraction (XRD) studies together with transmission electron microscopy

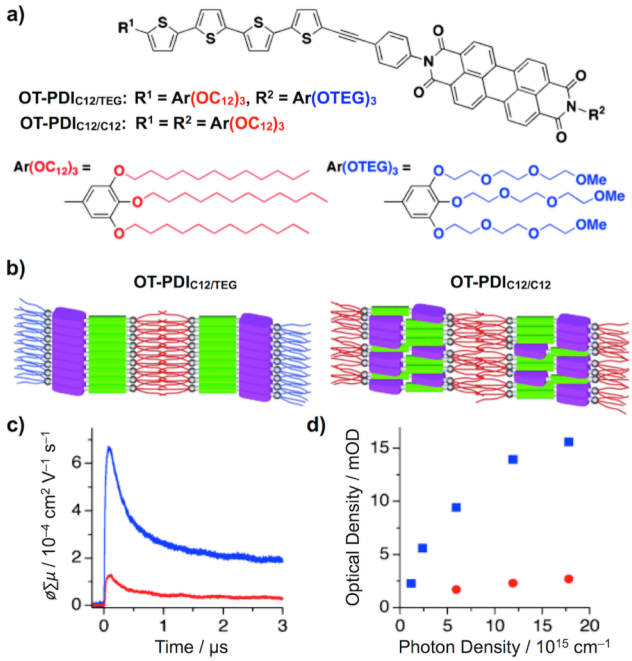

Fig. 9 (a) Molecular structures of $\textbf{OT-PDI}_{C12/TEG}$ and $\textbf{OT-PDI}_{C12/C12}$. (b) Proposed molecular packing geometries of the nanofiber of $\textbf{OT-PDI}_{C12/TEG}$ and microfiber of $\textbf{OT-PDI}_{C12/C12}$. (c) FP-TRMC profiles ($\lambda_{ex}$ = 355 nm, photon intensity = 1.2×10^{16} photons cm^{-2}). (d) Plots of changes in transient absorption intensity (ΔOD) at 720 nm versus photon density. Reproduced with permission from ref. 106. Copyright 2010 Wiley-VCH Verlag GmbH & Co. KGaA

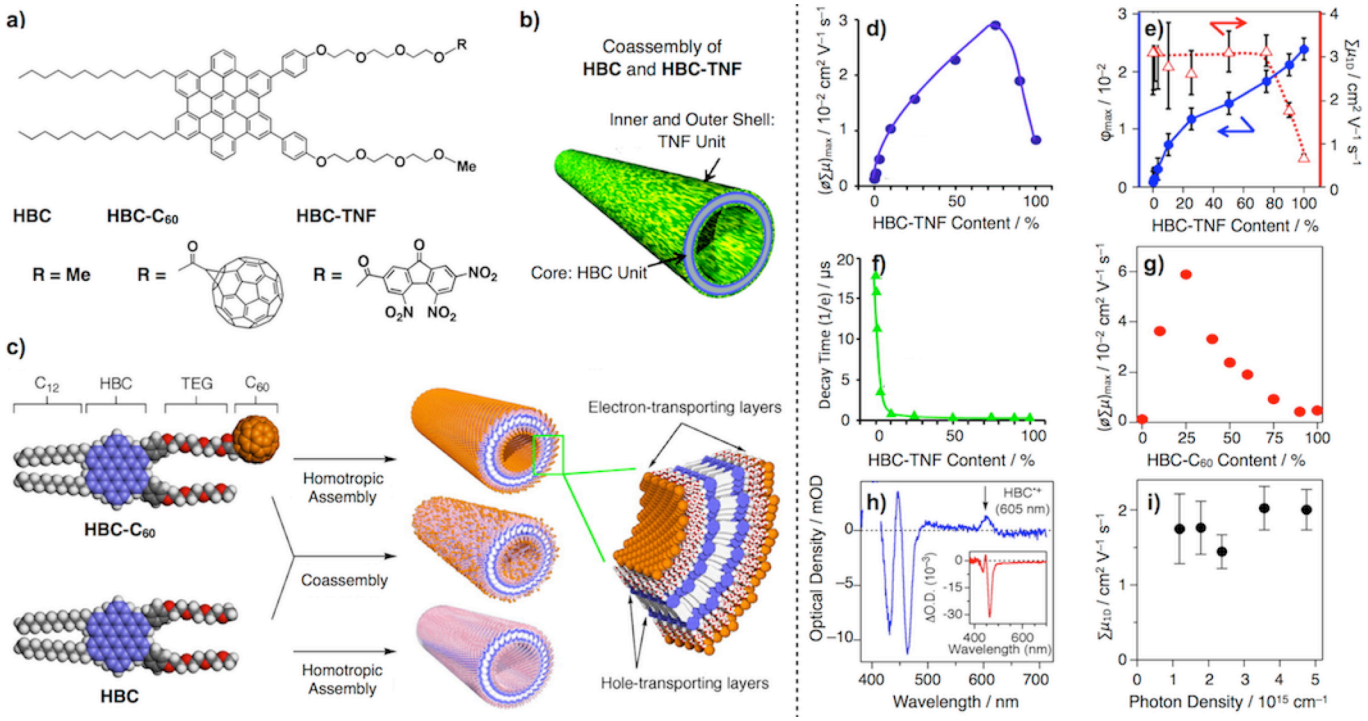

Fig. 10 (a) Molecular structures of **HBC**, **HBC-C$_{60}$** and **HBC-TNF**. (b) Schematic drawing of a coassembled nanotube consisting of **HBC** and **HBC-TNF**. (c) Schematic drawings of the formation of homotropic and coassembled nanotubes of **HBC** and **HBC-C$_{60}$**. (d) Plots of the maximum transient photoconductivity $(\phi\Sigma\mu)_{max}$ of the coassembled nanotubes of **HBC** and **HBC-TNF** as a function of **HBC-TNF** content (λ_{ex} = 355 nm, photon density = 4.7 × 10^{15} photons cm^{-2}). (e) Plots of ϕ_{max} (closed circles) estimated from TAS of HBC radical cation and 1D local charge carrier mobility $\Sigma\mu_{1D}$ (open triangles) as a function of **HBC-TNF** content. (f) Lifetime (1/e) dependence on **HBC-TNF** content. (g) Plots of $(\phi\Sigma\mu)_{max}$ of the coassembled nanotubes of **HBC** and **HBC-C$_{60}$** as a function of **HBC-C$_{60}$** content (λ_{ex} = 355 nm, photon density = 1.2 × 10^{15} photons cm^{-2}). (h) FP-TAS of a cast film of the coassembled nanotube with **HBC-C$_{60}$** content of 10%. (Inset) FP-TAS of a cast film of the homotropic nanotube of **HBC**. (i) Plots of $\Sigma\mu_{1D}$ versus photon density. Reproduced with permission from ref. 57 for (b), (d)–(f) and ref. 56 for (c), (g)–(i). Copyright 2011 American Chemical Society and 2009 National Academy of Sciences.

(TEM) and atomic force microscopy (AFM) observations revealed that a well-defined hexagonal columnar (Col_h) structure was formed by solution casting of the fibrous assemblies. Interestingly, upon thermal annealing at 200 °C, **CAPBI**·**M1** underwent a structural transition from Col_h to the thermodynamically more stable lamellar (Lam) structure, which was thought to be mainly triggered by the crystallization of PBI units. Of further interest, a **CAPBI**·**M1** film adopting a Lam structure showed, upon photoexcitation with a laser pulse, an obvious transient conductivity ($\varphi\sum\mu$), exhibiting a maximum value larger than that of a Col_h film (Fig. 8c). Considering the much smaller observed conductivity for **CAPBI** or **M1** alone, **CAPBI** and **M1** in the assembly gave rise to an efficient photo-induced charge separation and generation of mobile charge carriers, which was clearly confirmed by monitoring the PBI radical anion using TAS analysis (Fig. 8d). Given the carrier generation efficiency values obtained by TAS (φ) of 2.0 × 10^{-3} and 0.93 × 10^{-3} for the Lam and Col_h films, respectively, the sum of the mobility values ($\sum\mu$) were evaluated as 0.25 and 0.20 cm^2 V^{-1} s^{-1}, respectively. The observed difference in semiconducting properties possibly originates from structural dissimilarities; the Lam structure provides larger contact areas between PBI and alcoxyphenyl moieties (Fig. 8a), which results in higher photoinduced charge separation efficiencies.

Li, Fukushima, Aida *et al.* reported novel oligothiophene (OT)-perylenediimide (PDI) dyad molecules, **OT-PDI$_{C12/TEG}$** and **OT-PDI$_{C12/C12}$** (Fig. 9a), demonstrating the fabrication of a donor–acceptor fibrous assembly in a more controlled manner.[106] Due to the site-specific introduction of hydrophobic and hydrophilic tails, **OT-PDI$_{C12/TEG}$**, upon heating–cooling treatment in THF/MeOH, was shown to self-assemble into well-defined nanofibers with bicontinuous OT-PDI arrays (Fig. 9b), as determined through TEM observation and XRD analysis. In sharp contrast, **PDI$_{C12/C12}$** formed ill-defined microfibers with lamellar structures involving OT-PDI contacts, as evidenced by absorption spectroscopy. Using FP-TRMC and TAS methods similarly as described above, we confirmed the larger conductivity ($\varphi\sum\mu$) and carrier generation efficiency (φ) for the nanofiber of **OT-PDI$_{C12/TEG}$** compared to the microfiber of **OT-PDI$_{C12/C12}$** (Fig. 9c and d); these observations suggest the efficient charge separation between OT and PDI and subsequent carrier oscillation along OT/PDI stacked arrays in **OT-PDI$_{C12/TEG}$**, whereas the fast charge recombination may take place in **OT-PDI$_{C12/C12}$** due to the presence of the interdigitated OT/PDI structure.

Nanotubes

Nanotubes are nano-objects with greater structural definition than nanofibers; as such, molecular design strategies to obtain supramolecular nanotubes can be quite different from those used for nanofibers. Although several examples of self-assembled nanotubes from semiconducting π-electronic systems have been reported in recent years,[107–110] pioneering works containing detailed TRMC studies were demonstrated by Fukushima, Aida *et al.* As described in the previous section, they developed Gemini-shaped hexabenzocoronene (HBC) amphiphiles (**HBC**; Fig. 10a) that self-assemble into well-defined nanotubular objects,[58,59] whose walls consist of a graphitic hole-transporting layer of π-stacked HBC and whose inner and outer surfaces are covered by hydrophilic triethylene glycol (TEG) chains. In their representative example, by taking advantage of the TEG termini enabling easy functionalization, they synthesized HBC amphiphiles **HBC-C$_{60}$** and **HBC-TNF** carrying the electron-acceptor molecules C_{60} and trinitrofluorenone (TNF), respectively (Fig. 10a).[63,111] In appropriate conditions, **HBC-C$_{60}$** and **HBC-TNF** also self-assembled into bilayer-based nanotubes in a similar fashion as with **HBC**. In addition, they could co-assemble with **HBC** over a wide range of mixing molar ratios, resulting in a tunable acceptor density on the tubular surfaces.[112] Our group has analyzed in detail the carrier transporting properties along a single nanotubular axis.[64] In an **HBC**/**HBC-TNF** co-assembled nanotube system, the maximum transient conductivity $(\varphi\sum\mu)_{max}$ increased as **HBC-TNF** content was increased up to 80% (Fig. 10d), mainly originating from the increasing HBC-TNF contact allowing efficient photoinduced charge separation. However, a further increase in **HBC-TNF** content caused a significant decrease in conductivity derived from lower μ values (Fig. 10e), probably due to the poor structural integrity of the π-stacked HBC arrays as evidenced by SEM and TEM observations. At the same time, the lifetime of the photochemically generated charge carriers became lower in the presence of an acceptor (Fig. 10f), which can be explained by frequent charge recombination events. Replacement of TNF by C_{60} affords electron transport pathways that are hardly formed in the **HBC-TNF** system. In fact, **HBC-C$_{60}$** co-assembled nanotubes display *n*-type FET character as well as photovoltaic response. The bulkiness of C_{60} molecules results in an optimized transient conductivity at an **HBC-C$_{60}$** content of only 25% (Fig. 10g), consistent with the case of the **HBC**/**HBC-TNF** co-assembly. Worthy of note is that these co-assembled donor–acceptor nanotubes exhibited very high mobility values of $\sum\mu$ = 2–3 cm^2 V^{-1} s^{-1} as assessed by TAS (Fig. 10h) in appropriate mixing ratios (Fig. 10e and i), which is one of the best recorded among carbon-based soft materials and almost the same as the intersheet mobility in graphite.

Insulated molecular wires

Elaborate molecular design enables the development of insulated molecular wires[113–115] that have an ultimately well-defined one-dimensional carrier transport pathway. For example, Sugiyasu, Takeuchi *et al.* reported self-threading

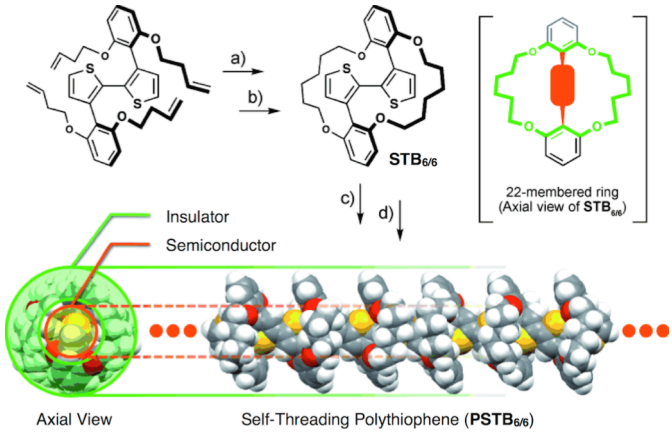

Fig. 11 Synthetic approach toward self-threading polythiophene: a) second-generation Grubbs catalyst, CH_2Cl_2, b) H_2, Pd/C, CH_2Cl_2/MeOH, c) NBS, $CHCl_3$/AcOH, d) [Ni(cod)$_2$], cod, bipy, toluene/DMF. "Cyclic side-chain" (green area in the axial view) corresponds to a 22-membered ring in the case of **STB$_{6/6}$**. NBS = *N*-bromosuccinimide, DMF = *N*,*N*-dimethylformamide, cod = 1,5-cyclooctadiene, bipy = 2,2′-bipyridine. Reproduced with permission from ref. 117. Copyright 2012 Wiley-VCH Verlag GmbH & Co. KGaA.

oligothiophenes and polythiophenes that are synthesized from bithiophene monomers having cyclic insulating chains (Fig. 11).[116–118] Because of the well-designed cyclic side chains, the polythiophene backbone cannot stack together, and instead adopts a highly planar conformation with a large effective conjugation length, as verified by absorption spectroscopy. Namely, charge carriers, if generated, can transport only along the main chains. In fact, soluble **PSTB$_{6/6}$** derivatives bearing two dodecyl groups in one monomer unit, upon I_2 doping, showed low conductivity (2×10^{-3} S cm^{-1}) in a four-probe measurement, probably due to the limited interchain transfer integral of π-electrons. However, the intrachain hole mobility of the soluble **PSTB$_{6/6}$** was revealed to be 0.9 cm^2 V^{-1} s^{-1}, as evaluated by FP-TRMC.

Terao *et al.* reported polyrotaxane-based soluble semiconducting molecular wires covered with insulating permethylated α-cyclodextrins (α-CDs) (Fig. 12).[119–121] In a crystal structure of a model compound, the phenylene ethynylene–based π-system was clearly observed to be accommodated within α-CD via host–guest interactions (Fig. 12a). In a typical case utilizing poly(phenylene ethynylene) main chains, insulating effects on the hole-transporting event along the backbones were discovered by an FP-TRMC technique (Fig. 12b and c). In conjunction with TAS measurements, the intrachain hole mobilities of **PPE$_{in}$** and **PPE$_{out}$** were found to be 0.7 and 0.2 cm^2 V^{-1} s^{-1}, respectively. The observed higher mobility suggests a smaller reorganization energy, while the longer lifetime of charge carriers may represent the suppression of interchain charge recombination, both of which are realized by the insulating matrix coating. Furthermore, they proposed a novel design principle addressing the ideal orbital alignment for charge carrier hopping.[122] Based on the theory, they developed a novel **PPE$_{m3}$** system with a zigzag main-chain configuration and confirmed that **PPE$_{m3}$**

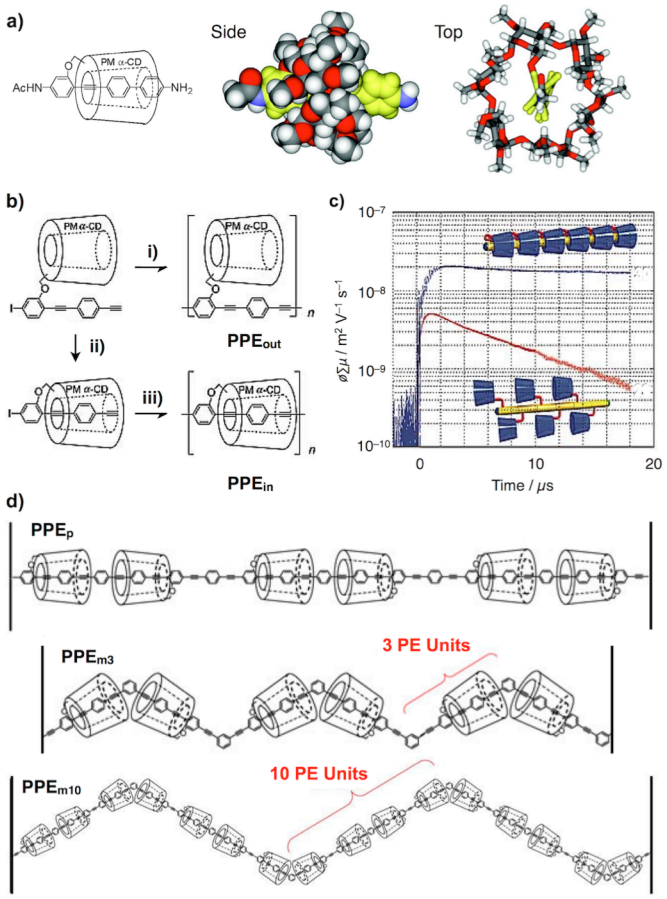

Fig. 12 (a) Molecular and crystal structure of a model rotaxane compound. (b) Synthetic approach toward poly(*p*-phenylene ethynylene)-based IMWs: i) $PdCl_2(PPh_3)_2$, CuI, K_2CO_3, *i*$PrNH_2$, ii) H_2O/MeOH, iii) $Pd(OAc)_2$, TXPTS, CuI, K_2CO_3, H_2O/MeOH. TXPTS = tris(2,4-dimethyl-5-sulfophenyl)phosphine trisodium salt. (c) Conductivity transients observed for a 2.3-μm thick cast film of $\mathbf{PPE_{out}}$ (red) and $\mathbf{PPE_{in}}$ (blue) (λ_{ex} = 355 nm, photon density = 7.3×10^{15} photons cm^{-2}). (d) Molecular structures of $\mathbf{PPE_p}$, $\mathbf{PPE_{m3}}$, and $\mathbf{PPE_{m10}}$. Reproduced with permission from ref. 121 for (a)–(c) and ref. 122 for (d). Copyright 2011 Wiley-VCH Verlag GmbH & Co. KGaA and 2013 Macmillan Publishers Ltd.

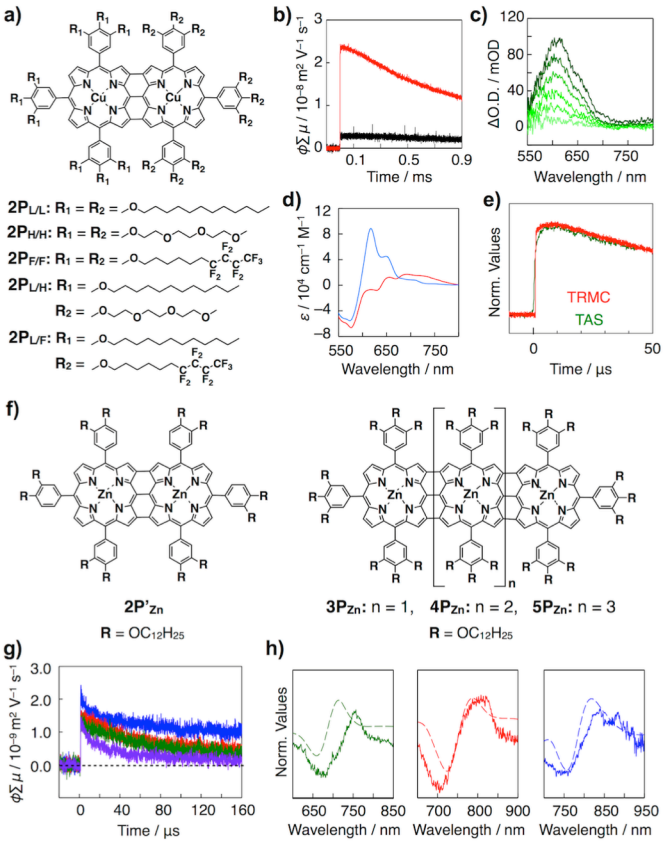

Fig. 13 (a) Molecular structures of triply-fused copper porphyrin dimers. (b) FP-TRMC profiles of $\mathbf{2P_{L/H}}$ (red) and $\mathbf{2P_{L/L}}$ (black) films on a quartz (λ_{ex} = 355 nm, photon density = 1.2×10^{16} photons cm^{-2}). (d) Differential absorption spectra upon generation of the radical cation (red) in CH_2Cl_2 and anion (blue) in THF of $\mathbf{2P_{L/H}}$. (e) Normalized decay profiles of FP-TRMC (red) and 620-nm transient absorption (green) of $\mathbf{2P_{L/H}}$. (c) FP-TAS profiles of $\mathbf{2P_{L/H}}$ (λ_{ex} = 355 nm, photon density = $1.2–7.2 \times 10^{16}$ photons cm^{-2}; from light green to green). (f) Molecular structures of liquid crystalline triply-fused zinc porphyrin oligomers $\mathbf{2P'_{Zn}}$, $\mathbf{3P_{Zn}}$, $\mathbf{4P_{Zn}}$ and $\mathbf{5P_{Zn}}$. (g) FP-TRMC profiles of $\mathbf{2P'_{Zn}}$ (purple), $\mathbf{3P_{Zn}}$ (green), $\mathbf{4P_{Zn}}$ (red) and $\mathbf{5P_{Zn}}$ (blue) films on a quartz (λ_{ex} = 355 nm, photon density = 0.9×10^{16} photons cm^{-2}). (h) Normalized profiles of TAS (solid) and differential absorption spectra upon generation of the radical cations (dashed) of $\mathbf{3P_{Zn}}$ (green), $\mathbf{4P_{Zn}}$ (red) and $\mathbf{5P_{Zn}}$ (blue).

showed a higher hole mobility of 2.1 $cm^2\ V^{-1}\ s^{-1}$ ($\mathbf{PPE_p}$: 0.7 $cm^2\ V^{-1}\ s^{-1}$). Surprisingly, when 10 phenylene ethynylene units were employed as a repeating unit in the zigzag main chains ($\mathbf{PPE_{m10}}$), the hole mobility reached up to 8.5 $cm^2\ V^{-1}\ s^{-1}$, which is also supported by the theoretical study.

Liquid crystals

Thermotropic liquid crystals (LC) are a kind of bulk-phase material displaying 1D (columnar phase) and 2D (smectic phase) formations,[123–125] which provide directional charge carrier transport pathways since LC phases are organized via supramolecular interactions among the constituent molecules. Characterization of charge-carrier transport properties in LC materials is often performed through TOF, SCLC, and FET techniques,[126–128] which analyses long-range carrier motions as discussed in detail in Section 2. TRMC methods provide local-scale carrier dynamics within intracolumnar or intralayer structures. In fact, after the discovery of fast electrical conduction along the columnar axis,[129,130] Warman *et al.* demonstrated the mobility evaluation of LC materials by means of PR-TRMC methods.[131,132] Recently, Aida *et al.* reported many nonconventional discotic LC molecules and performed FP-TRMC studies through collaborations with our groups.[133–135] For example, they used triply-fused porphyrin oligomers as extra-large tape-like mesogens.[136–138] Although both $\mathbf{2P_{L/L}}$ and $\mathbf{2P_{H/H}}$, decorated at their peripheries with hydrophobic or hydrophilic chains, did not show any LC mesophase (Fig. 13a), the site-specific modification by these two immiscible chains allowed the dimeric core ($\mathbf{2P_{L/H}}$) to self-assemble into a rectangular columnar mesophase, induced by nano-segregation of the two immiscible chains. As expected from the structural differences, $\mathbf{2P_{L/H}}$, forming one-dimensional columnar structures, exhibited a much higher conductivity in FP-TRMC

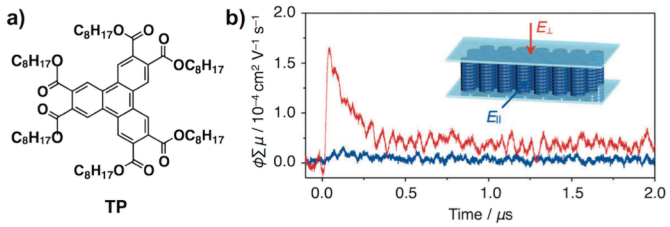

Fig. 14 (a) Molecular structures of triphenylene hexacarboxylic ester (**TP**) (b) FP-TRMC profiles of a LC film of **TP** sandwiched by quartz plates at 25 ºC, observed along parallel (blue) and perpendicular (red) directions to the substrate surface. Reproduced with permission from ref. 141. Copyright 2012 Wiley-VCH Verlag GmbH & Co. KGaA.

(Fig. 13b). Of further interest, $\mathbf{2P_{L/H}}$ showed a clear transient absorption at around 620 nm (Fig. 13c) assignable to the absorption of radical anion $\mathbf{2P_{L/H}}^{\bullet-}$, which was confirmed by chemical oxidation/reduction experiments in solution (Fig. 13d). Considering the fact that the kinetic profiles of TRMC and TAS (at 620 nm) signals are in agreement (Fig. 13e), the charge carrier species of $\mathbf{2P_{L/H}}$ was found to be the electron (μ_e = 0.2 $cm^2\ V^{-1}\ s^{-1}$), whereas almost all other reported monomeric porphyrins behaved as hole-transporting materials. A few years later, they disclosed the hole-transporting properties of columnar liquid crystalline $\mathbf{2P_{F/F}}$. The substitution pattern of the peripheral chains barely changed the intrinsic π-electronic properties of the dimeric porphyrin core, but transformed the π-stacking geometry, as clarified by UV-vis absorption spectroscopy. Thus, they proposed that the observed difference in polarity of the charge carriers originates from the different orbital overlaps within π-stacked columns; in fact, a theoretical prediction has been made in relation to this possibility.[139,140] Thereafter, by screening various substitution patterns, they found that two-to-five mer Zn complexes, if having an optimum number of long alkyl chains in proper positions ($\mathbf{2P'_{Zn}}$, $\mathbf{3P_{Zn}}$, $\mathbf{4P_{Zn}}$, and $\mathbf{5P_{Zn}}$), could form LC materials (Fig. 13f), where the transient conductivity in TRMC becomes larger as the core size is enlarged (Fig. 13g). In this series, they concluded that the hole is the dominant charge carrier species (μ_h = 0.02 $cm^2\ V^{-1}\ s^{-1}$ for $\mathbf{5P_{Zn}}$), since TAS experiments adequately explain their spectral similarity with the absorption bands of the corresponding radical cation species (Fig. 13h).

Although TRMC-based techniques, in principle, provide nanometer-scale mobilities, we can evaluate the anisotropy in carrier transport directions in macroscopically-aligned LCs.[141,142] Fukushima, Aida *et al.* reported a novel triphenylene-based columnar LC molecule (**TP**), whose hexagonal columns were observed to have high homeotropic alignment on/between a large variety of substrates (Fig. 14a).[141] When sandwiched between two quartz plates and allowed to cool from the isotropic phase to 25 °C, **TP** perfectly aligned homeotropically with large domains, as confirmed by polarized optical microscopy. By changing the insertion direction of the sandwiched LC sample in the cavity as well as the excitation-laser direction in FP-TRMC, we can selectively monitor charge carrier transport phenomena along the electric field of the

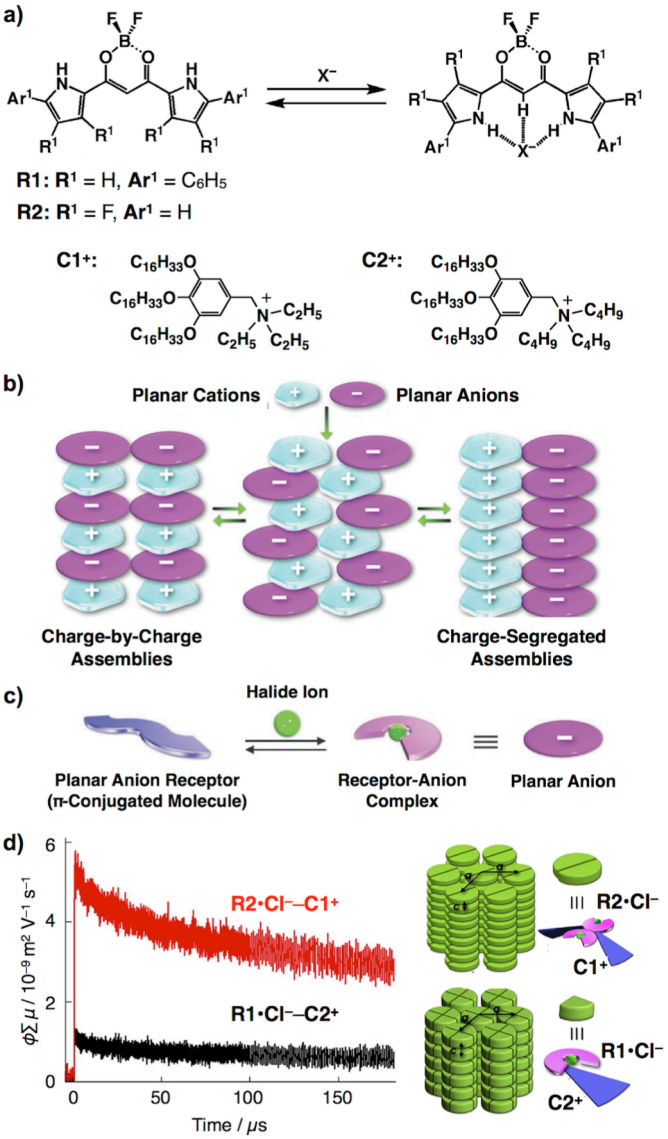

Fig. 15 (a) Molecular structures of anion receptors **R1** and **R2** and their anion-binding mode. Structures of cation modules $\mathbf{C1^+}$ and $\mathbf{C2^+}$. (b) Schematic illustrations of charge-by-charge and charge-segregated assemblies. (c) Formation of planar anionic species through complexation of planar anion receptors with halide ions. (d) FP-TRMC profiles of $\mathbf{R1{\cdot}Cl^-}$–$\mathbf{C2^+}$ (black) and $\mathbf{R2{\cdot}Cl^-}$–$\mathbf{C1^+}$ (red) (λ_{ex} = 355 nm, photon density = 0.9×10^{16} photons cm^{-2}) and schematic illustration of their hexagonal columnar structures. Reproduced with permission from ref. 143 for (b), (c) and ref. 147 for (d). Copyright 2013 The Royal Society of Chemistry and 2013 American Chemical Society.

microwave. In fact, the above macroscopically oriented **TP** film displayed highly anisotropic conductivity profiles (Fig. 14b). As demonstrated here, we can easily carry out the experimental verification of such a relationship between macroscopic structure and charge carrier mobility by using the FP-TRMC system.

Maeda *et al.* reported a novel anion-responsive structural motif consisting of boron complexes of 1,3-dipyrrolyl-1,3-propanediones (Fig. 15a), and proposed "charge-by-charge assembly" and "charge-segregated assembly"

concepts (Fig. 15 b).[143,144] Upon complexation with chloride ion, the receptor undergoes a structural transition into a negatively-charged planar species (Fig. 15c) and mainly forms the charge-by-charge assembly with the corresponding counter cations via electrostatic interactions. When functionalized with long alkyl tails at the periphery of the receptor, such an assembly affords thermotropic columnar LC materials in their condensed phases.[145,146] However, evidence of charge-segregated assembly was sometimes observed in particular cases. For example, they prepared anion receptors **R1** and **R2** as well as quaternary ammonium chloride salt derivatives with long alkyl chains (**C1**$^+$·Cl$^-$ and **C2**$^+$·Cl$^-$) and attempted complexations between them.[147] As a result, they found that **R2**·Cl$^-$–**C1**$^+$ and **R1**·Cl$^-$–**C2**$^+$ successfully formed a columnar LC material with receptor-anion complexes, in which the former contains charge-segregated assemblies while the latter consists of charge-by-charge assemblies (Fig. 15d), as evidenced by the stacking periodicity observed in XRD experiments. This supramolecular structural difference resulted in a high contrast in charge carrier transporting properties, clearly demonstrated by FP-TRMC measurements (Fig. 15d). After estimation of φ values using a direct current method,[148,149] TRMC mobility values were determined as $\sum\mu$ = 0.2 and 0.05 cm^2 V^{-1} s^{-1} for **R2**·Cl$^-$–**C1**$^+$ and **R1**·Cl$^-$–**C2**$^+$, respectively.

Overall, the combination of FP-TRMC and TAS techniques is quite effective for evaluating charge carrier mobility in molecular materials including single crystals, polycrystals, gels, liquid crystals, and other soft materials. As summarized above, TRMC results often reflect the structural differences on both a nanoscopic and macroscopic scale, thus representing a powerful tool for investigating the structural–conductivity relationship in solid-state materials.

5. Electron spin resonance as a probe of charge-carrier transporting phenomena

In the previous sections, we introduced studies on charge transport properties using TRMC methods. Alternatively, electron spin resonance (ESR), one of the most common microwave spectroscopic methods, has also been used for studying electrically conductive materials for decades,[150] particularly in the fields of inorganic semiconductors[151,152] and conductive polymers.[153–156] ESR spectroscopy has characteristic features in common with the TRMC method as follows: 1) non-contact measurements are performed using microwaves as a probe; 2) microscopic information about spins (or charge carriers for the TRMC method) can be obtained; 3) the techniques are widely applicable to the characterization of solid materials independent of their morphology. By using ESR spectroscopy, we can directly observe polarons, a paramagnetic charge carrier species that play an important role in electric conduction phenomena. In this section, we introduce recent applications of ESR for studies of carrier transport properties of organic materials.

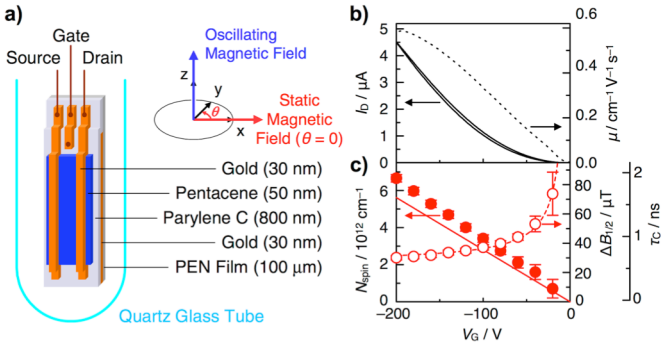

Fig. 16 (a) Structure of undoped pentacene thin-film transistor (TFTs) and the magnetic field geometries. θ is the angle made by the device film and the static magnetic field. (b) Transfer characteristic (solid line) and field-effect mobility μ (dotted line) of undoped pentacene TFT at V_D = –1 V. (c) The number of spins (N_{spin}, solid circle) and the line width ($\Delta B_{1/2}$, open circle) estimated from the field-induced ESR spectra. The solid line represents the estimation of carrier number by the electrostatic capacitance. The second right-hand axis shows τ_c. Reproduced with permission from ref. 159. Copyright 2008 the American Physical Society.

ESR of field-induced polarons in organic devices

Marumoto *et al.*[33,157,158] and Matsui *et al.*[159–161] applied ESR methods to investigate the motions of gate-induced charge carriers in organic field-effect devices. Fig. 16a shows a typical setting for the field-induced ESR (FI-ESR) measurement of organic FET devices. The target device is fabricated on a slim substrate and inserted in a quartz glass tube, which is then installed in an ESR spectrometer. Applying the gate voltage (V_G) leads to an ESR signal derived from the field-induced charge carriers (polarons) at the insulator–semiconductor interface. The spectral shape of the FI-ESR contains a large amount of microscopic information about the polarons in the device: the number of polarons, the nuclear environment around the polarons, the orientations of the molecules in the crystal, *etc*. In particular, the line width of the ESR spectrum is highly important because the spatial extent of the delocalized spins and/or motion of the spins in the materials directly affects the line width. The fast diffusion of polarons in the materials makes the line width narrower (motional narrowing).[162] The motional narrowing effects were clearly observed in both pentacene polycrystalline film transistors[159] and rubrene single-crystal transistors;[158] these results were analyzed based on the multiple trap-and-release (MTR) transport mechanism, which postulates that the charge carriers are hopping from trap to trap. The average times at traps were estimated to be 0.7–2 ns (for the polycrystalline pentacene FET, Fig. 16c) and ~60 ps (for the rubrene single-crystal FET after SAM treatment), which is consistent with the fact that the mobility of the rubrene FET is higher than that of the pentacene FET. Matsui *et al.* extensively investigated the energetic landscape of trap sites in pentacene thin-film transistors at low temperatures.[160] From the line width analyses using eqn (22), they concluded that there exist three kinds of traps composed of localized wave

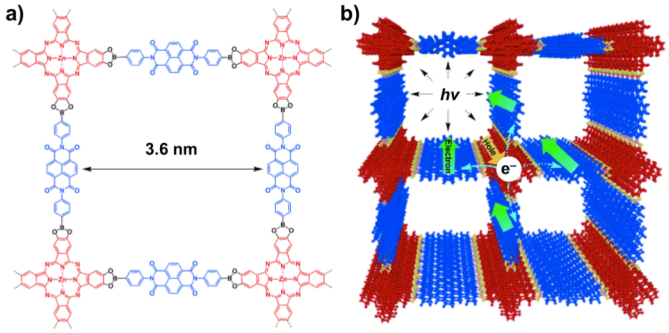

Fig. 17 (a) Donor–acceptor COF ($\mathbf{D_{ZnPc}}$-$\mathbf{A_{NDI}}$-**COF**). Donor and acceptor units are shown in red and blue, respectively. (b) Illustration of a 2 × 2 cell of the 0.8 Å slipped stacked COFs and photochemical events. Reproduced with permission from ref. 168. Copyright 2013 Wiley-VCH Verlag GmbH & KGaA.

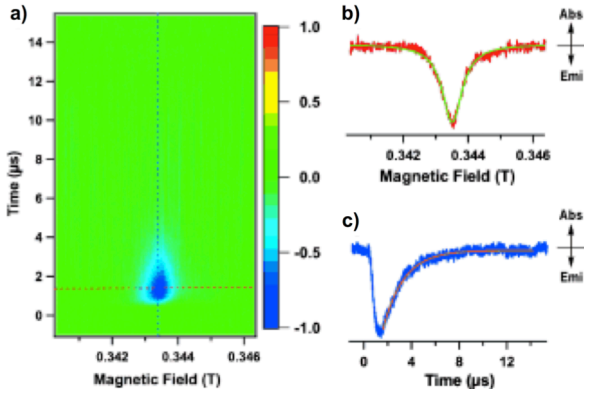

Fig 18 (a) Counter plots of the TR-ESR spectrum of the solid-state COF at 280 K. The transverse and longitudinal axes denote time and magnetic field, respectively. The normal axis is the TR-ESR intensity. The negative and positive signs of signal intensity indicate the absorption and emission of the microwaves, respectively. (b) Time slice of the TR-ESR spectrum at t = 1.5 μs. The green line is the curve calculated based on the Lorentz function. (c) Time profile of the curve calculated based on the exponential function $\Phi = \alpha\exp[-t/\tau_{CS}]$. Reproduced with permission from ref. 168. Copyright 2013 Wiley-VCH Verlag GmbH & KGaA.

functions spanning around 1.5, 5, and 6–20 molecules. Using diagrammatic Monte Carlo (DMC) calculations for the Holstein model,[163] they evaluated the binding energies of these traps to be 140 meV, 22 meV and 5–15 meV, respectively.

Time-resolved ESR as a probe of charge dynamics

Photoconduction has attracted much attention in relation to the recent remarkable developments in organic photovoltaic (OPV) devices.[164] In this context, understanding the mechanism of photo-induced electron transfer from the donor–acceptor interface is highly important for achieving high-performance OPV devices. During the first stage of photo-induced electron transfer, a charge-separate (CS) state composed of a radical cation of the donor ($D^{\bullet+}$) and a radical anion of the acceptor ($A^{\bullet-}$) could be generated; therefore, an ESR-based method would be a strong investigative tool for this process.[165,166] Time-resolved ESR (TR-ESR),[167] one of the established ESR methods, can probe the radical pair generated by a laser flash, which may provide insight into the dynamics of the primary process.

This method was applied to the photoinduced electron transfer process in a donor–acceptor covalent organic framework (COF) consisting of zinc phthalocyanine (ZnPc) and naphthalene diimide (NDI) as the electron donor and acceptor, respectively (Fig. 17).[161] The donor–acceptor COFs consist of a periodically ordered bicontinuous heterojunction structure and self-sorted donor and acceptor columnar arrays with well-defined intervals on the nanometer scale.[162] This nanoscopic segregation morphology forms a broad interface for charge separation and provides ambipolar pathways for charge collection, ideal characteristics for OPV devices. Fig. 18 shows the TR-ESR spectrum of the donor–acceptor COF at 700 nm excitation. Prior to the laser flash, the sample was ESR-silent over the entire magnetic range (Fig. 18a, t < 0 μs). After the laser flash, the TR-ESR signal rapidly increased as a result of a prompt charge separation (Fig. 18a) and exhibited an increase up to t = 1.5 μs followed by slow decay. The TR-ESR signal at t = 1.5 μs was reproduced with a single emission-type Lorentzian with a g value of 2.0059 and a narrow spectral width of 0.75 mT (Fig. 18b). The narrow spectral width of the COF is consistent with a weak magnetic dipolar interaction between two spins, as they are separately delocalized over donor and acceptor columns. The time-profiles of the TR-ESR signals (Φ) were reproduced by an exponential function,

$$\Phi = \alpha\exp(-t/\tau_{CS}), \quad (25)$$

where α, t, and τ_{CS} are the proportional factor, time, and lifetime, respectively; the τ_{CS} values of the COFs at 280 K and 80 K were determined to be 1.8 μs and 1500 μs, respectively (Fig. 18c). These long lifetimes indicate that the aligned bicontinuous π-columns enable long-distance charge delocalization and exceptional long-term charge retention. The quantitative analysis of charge carrier mobility in the COF systems was also reported as their nanometer scale motion,[170,171] suggesting the promotion of highly conducting pathways along the π-columns via their strong stacking nature.

Evaluation of intramolecular conductance by ESR

Conjugated molecular wires are attracting interest in the field of molecular electronics, making it important to clarify the intra-chain mobility of these wires. However, it is generally difficult to measure the conductivity of a single molecule or a polymer chain by conventional device characterization, with the exception of nano-gap electrodes or a break-junction technique with a scanning tunnelling microscope (STM). Using the FP-TRMC method, our group has measured the intra-chain charge carrier mobility of conjugated polymers dispersed in an insulating matrix[172] and novel polymers encapsulated by cyclic side chains[116] or permethylated α-cyclodextrin.[119,122] Meanwhile, Matsuda *et al.* proposed a unique approach to evaluate intra-molecular conductance with ESR.[173,174] The conductive property of a molecular wire is characterized by the

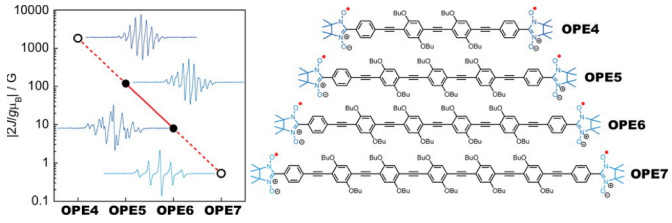

Fig. 19 (left) X-band ESR spectra measured at room temperature for **OPE4-7**. (right) Molecular structures of **OPE4-7**. Reproduced with permission from ref. 174. Copyright 2013 American Chemical Society.

decay constant β of electron tunnelling, which is defined according to the following equation:

$$G = G_0 \exp(-\beta l), \qquad (26)$$

where G is the conductance of the molecule, l is the molecular length, and G_0 is the contact conductance. Not only does the conductance of the molecule decay exponentially according to eqn (26), but also the rate constant of electron transfer (k)[175] and exchange interaction (J)[176,177] between radical spins. Matsuda *et al.* experimentally[173,177] and theoretically[178] determined the decay constant of the exchange interaction between radical spins of neutral radicals placed at the two ends of a π-conjugated wire. In these studies, they synthesized rod-like oligo(*p*-phenylene) (OP)[173] and oligo(*p*-phenylene ethynylene) (OPE)[174] molecules having different lengths, which were substituted with nitronyl nitroxide radicals at the two ends (Fig. 19). A magnetically independent nitronyl nitroxide shows a 5-line ESR spectrum with a 7.5 G line spacing resulting from two identical nitrogen atoms. When two nitronyl nitroxides are magnetically coupled with a larger exchange interaction than the hyperfine coupling constants, the diradical gives a nine-line ESR spectrum with a 3.7 G spacing. If the exchange interaction is smaller than the hyperfine coupling in the diradical, two nitronyl nitroxide radicals are magnetically independent and show a spectrum identical to the nitronyl nitroxide monoradical. In the intermediate situations, the spectrum shows further splitting, which could be reproduced by ESR simulations. Fig. 19 shows the results of ESR measurements of the OPE wires consisting of four to seven *p*-phenylene ethynylene (PE) units in dichloromethane solution. The shortest one (**OPE4**) showed a nine-line ESR spectrum, meaning that the exchange interaction is larger than the hyperfine coupling constant. The ESR spectra of **OPE5** and **OPE6** showed 15 lines. The **OPE7** showed a five-line ESR spectrum, which means that the exchange interaction in **OPE7** is smaller than the hyperfine coupling constant. From the ESR simulations, the values of the exchange interaction J of these wires were estimated, and the decay constant β of the OPE wires were calculated to be 0.39 Å^{-1}, in good agreement with the reported decay constant β from the molecular conductance (0.20–0.34 Å^{-1})[179–181] and reported theoretical values (0.19–0.27 Å^{-1}).[182,183] The decay constant β of the OP wires was also calculated to be 0.51 ± 0.01 Å^{-1} by the same method,[173] suggesting that the OPE wires have better conductive properties than the OP wires. As a characteristic feature of this method, the β value obtained by this ESR method reflects a pure tunnelling electron exchange and there is no participation of the hopping electron transfer, which is expected to appear in longer molecules such as OPE derivatives with more than three OPE units.[179]

Concluding remarks

Organic molecular materials and their supramolecular assemblies potentially contain an excessive amount of impurities, structural defects, and/or boundaries, which often perturb charge-carrier transport phenomena under an applied static electric field. The structural variation found in organic materials is substantially wider than that in inorganic semiconductor materials, suggesting the necessity of rapid techniques to screen materials for their mobility values in order to assess their feasibility as semiconductors.

Static and dynamic electric current analyses provide charge carrier mobilities as well as perturbing factors, and reflect their predicted performances *in device fabrication*. Dynamic analysis with electromagnetic waves allows us to derive the potentials of these materials with rapid protocols, which is advantageous in the primary assessment of organic semiconductor candidates with wide structural variation. TRMC and ESR measurements probe the local motion of charge carriers, revealing the effective mass of the charge carrier species and the feasibility of molecular systems toward "molecular scale" electronics. HE and TOF elucidate the translational motion of charge carriers as well as principal "thermal" effects on the transport, which may assist in providing control over disordering processes, clarifying dominant processes, and allow for devices functional at room temperature. FET and SCLC measurements address the primary interfacial events in charge carrier transport. Combined protocols based on the sophisticated and well-established techniques of HE, TOF, SCLC, FET, TRMC, ESR, *etc*. will be anticipated to play a key role in organic semiconductor development to substitute Si, compounds, and metal-oxide semiconductor materials. The presumed value of mobility in organic semiconductors, some of which have shown high enough values to substitute amorphous Si semiconductors, was already reported in the middle of the 20th century, and remained as "presumed over 60 years." We believe that the present-day concerted measurements of charge carrier mobility toward their optimization and substitution of traditional semiconductor materials for organic materials, some of which have been described here, will open the new era of organic electronics.

Acknowledgements

This work has been supported by KAKENHI from the Japan Society for the Promotion of Science (JSPS) and the Funding Program for Next Generation World Leading Researchers from

the Cabinet Office, Government of Japan. S.S. and A.S. thank the PRESTO program of the Japan Science and Technology Agency. T.S. and D.S. thank the JSPS for fellowships.

Notes and references

1 D. D. Elyey, *Nature*, 1948, **162**, 819.
2 H. Akamatu and H. Inokuchi, *J. Chem. Phys*., 1950, **18**, 810.
3 J. Ferraris, D. O. Cowan, V. Walatka and J. H. Perlstein, *J. Am. Chem. Soc.*, 1973, **95**, 948.
4 D. Jérome, A. Mazaud, M. Ribault and K. Bechgaard, *J. Phys. Lett.*, 1980, **41**, 95.
5 H. Shirakawa, E. J. Louis, A. G. MacDiarmid, C. K. Chiang and A. J. Heeger, *J. Chem. Soc., Chem. Comm*., 1977, 578.
6 A. Epstein and B. S. Wildi, *J. Chem. Phys.* 1960, **32**, 324.
7 P. G. Le Comber and W. E. Spear, *Phys. Rev. Lett*., 1970, **25**, 509.
8 G. Juska, K. Arlauskas and M. Viliunas, *Phys. Rev. Lett*., 2000, **84**, 4946.
9 H. Akamatsu, H. Inokuchi and Y. Matsunaga, *Nature,* 1954, **173**, 168.
10 N. Deprez and D. S. McLachlan, *J. Phys. D: Appl. Phys*., 1988, **21**, 101.
11 K. S. Novoselov, A. K. Geim, S. V. Morozov, D. Jiang, Y. Zhang, S. V. Dubonos, I. V. Grigorieva and A. A. Firsov, *Science*, 2004, **306**, 666.
12 T. Dulrkop, S. A. Getty, E. Cobas and M. S. Fuhrer, *Nano Lett*., 2004, **4**, 35.
13 P. A. M. Dirac, *Proc. R. Soc. A*, 1928, **117**, 610.
14 L. Friedman and T. Holstein, *Ann. Phys.*, 1963, **21**, 494.
15 I. Langmuir, *Phys. Rev.*, 1913, **2**, 450.
16 D. H. Dunlap, P. E. Parris and V. M. Kenkre, *Phys. Rev. Lett.*, 1996, **77**, 542.
17 W. D. Gill, *J. Appl. Phys*., 1972, **43**, 5033.
18 J. Frenkel, *Phys. Rev*., 1938, **54**, 647.
19 H. Bässler, *Phys., Status Solidi B*, 1993. **175**, 15.
20 S. Seki, Y. Yoshida, S. Tagawa, K. Asai, K. Ishigure, K. Furukawa, M. Fujiki and N. Matsumoto, *Philos. Mag*., 1999, **79**, 1631.
21 J. C. Slater, *Rev. Mod. Phys.*, 1946, **18**, 441.
22 A. Maeda, H. Kitano and R. Inoue, *J. Phys.: Condens. Matter*, 2005, **17**, R143.
23 J. M. Warman, M. P. de Haas and H. M. Wentinck, *Radiat. Phys. Chem.,* 1989, **34**, 581.
24 J. M. Warman, G. H. Gelinck and M. P. de Haas, *J. Phys.: Condens. Matter*, 2002, **14**, 9935.
25 F.C. Grozema, L. D. A. Siebbeles, J. M. Warman, S. Seki, S. Tagawa and U. Scherf, *Adv. Mater.*, 2002, **14**, 228.
26 A. Saeki, S. Seki, T. Sunagawa, K. Ushida and S. Tagawa, *Philos. Mag*., 2006, **86**, 1261.
27 A. Saeki, S. Seki, Y. Koizumi, T. Sunagawa, K. Ushida and S. Tagawa, *J. Phys. Chem. B*, 2005, **109**, 10015.
28 A. Saeki, Y. Koizumi, T. Aida and S. Seki, *Acc. Chem. Res.,* 2012, **45**, 1193.
29 S. Seki and S. Tagawa, *Polym. J*., 2007, **39**, 277.
30 A. Saeki, S. Seki, Y. Koizumi and S. Tagawa, *J. Photochem. Photobiol. A* 2007, **186**, 158.
31 A. Saeki, S. Ohsaki, S. Seki and S. Tagawa, *J. Phys. Chem. C*, 2008, **112**, 16643..
32 Y. Honsho, T. Miyakai T. Sakurai A. Saeki and S. Seki, *Sci. Rep*., 2013, **3**, 3182.
33 K. Marumoto, S. Kuroda, T. Takenobu and Y. Iwasa, *Phys. Rev. Lett*., 2006, **97**, 256603.
34 R. P. Ortiz, A. Facchetti and T. J. Marks, *Chem. Rev.*, 2010, **110**, 205.
35 K. Takimiya, S. Shinamura, I. Osaka and E. Miyazaki, *Adv. Mater.*, 2011, **23**, 4347.
36 T. Sekitani and T. Someya, *Jpn. J. Appl. Phys.*, 2012, **51**, 100001.
37 J. Mei, Y. Diao, A. L. Appleton, L. Fang and Z. Bao, *J. Am. Chem. Soc.*, 2013, **135**, 6724.
38 R. A. Marcus, *Rev. Mod. Phys.*, 1993, **65**, 599.
39 J. E. Anthony, *Chem. Rev.* 2006, **106**, 5028.
40 Y. Sakamoto, T. Suzuki, M. Kobayashi, Y. Gao, Y. Fukai, Y. Inoue, F. Sato and S. Tokito, *J. Am. Chem. Soc.*, 2004, **126**, 8138.
41 M. Watanabe, Y. J. Chang, S.-W. Liu, T.-H. Chao, K. Goto, Md. M. Islam, C.-H. Yuan, Y.-T. Tao, T. Shinmyozu and T. J. Chow, *Nat. Chem.*, 2012, **4**, 574.
42 C. D. Dimitrakopoulos and P. R. L. Malenfant, *Adv. Mater.*, 2002, **14**, 99.
43 J. Kang, M. Noh, D. S. Park, H. J. Kim and C. N. Whang, *J. Appl. Phys.*, 2004, **95**, 2293.
44 C. R. Newman, R. J. Chesterfield, M. J. Panzer and C. D. Frisbie, *J. Appl. Phys.*, 2005, **98**, 084506.
45 H. Yang, T. J. Shin, M.-M. Ling, K. Cho, C. Y. Ryu and Z. Bao, *J. Am. Chem. Soc.*, 2005, **127**, 11542.
46 S. Lee, B. Koo, J. Shin, E. Lee, H. Park and H. Kim, *Appl. Phys. Lett.*, 2006, **88**, 162109.
47 X.-H. Zhang, S. P. Tiwari, S.-J. Kim and B. Kippelen, *Appl. Phys. Lett.*, 2009, **95**, 223302.
48 S.-H. Wen, A. Li, J. Song, W.-Q. Deng, K.-L. Han and W. A. Goddard III, *J. Phys. Chem. B*, 2009, **113**, 8813.
49 A. Saeki, S. Seki and S. Tagawa, *J. Appl. Phys.*, 2006, **100**, 023703.
50 X. Feng, V. Marcon, W. Pisula, M. R. Hansen, J. Kirkpatrick, F. Grozema, D. Andrienko, K. Kremer and K. Müllen, *Nat. Mater.*, 2009, **8**, 421.
51 J. P. Hill, W. Jin, A. Kosaka, T. Fukushima, H. Ichihara, T. Shimomura, K. Ito, T. Hashizume, N. Ishii and T. Aida, *Science*, 2004, **304**, 1481.
52 W. Jin, Y. Yamamoto, T. Fukushima, N. Ishii, J. Kim, K. Kato, M. Takata and T. Aida, *J. Am. Chem. Soc.*, 2008, **130**, 9434.
53 Amsterdam Density Functional, Scientific Computing and Modelling, Theoretical Chemistry; Vrije University: Amsterdam, The Netherlands (http://www.scm.com).
54 E. F. Valeev, V. Coropceanu, D.A. da Silva Filho, S. Salman and J.-L. Brédas, *J. Am. Chem. Soc.*, 2006, **128**, 9882.
55 W. Q. Deng, and W. A. Goddard III, *J. Phys. Chem. B*, 2004, **108**, 8614.
56 Y. Yamamoto, G. Zhang, W. Jin, T. Fukushima, N. Ishii, A. Saeki, S. Seki, S. Tagawa, T. Minari, K. Tsukagoshi and T. Aida, *Proc. Natl. Acad. Sci.,* 2009, **106**, 21051.
57 A. Saeki, Y. Yamamoto, Y. Koizumi, T. Fukushima, T. Aida and S. Seki, *J. Phys. Chem. Lett.*, 2011, **2**, 2549.
58 J. Jortner, *J. Chem. Phys.,* 1976, **64**, 4860.

59 J.-L. Brédas, D. Beljonne, V. Coropceanu and J. Cornil, *Chem. Rev.,* 2004, **104**, 4971.
60 P. F. Barbara, T. J. Meyer and M. A. Ratner, *J. Phys. Chem.,* 1996, **100**, 13148.
61 E. Di Donato, R. P. Fornari, S. Di Motta, Y. Li, Z. Wang and F. Negri, *J. Phys. Chem. B*, 2010, **114**, 5327.
62 S. Di Motta, M. Siracusa and F. Negri, *J. Phys. Chem. C,* 2011, **115**, 20754.
63 S. Di Motta, E. Di Donato, F. Negri, G. Orlandi, D. Fazzi and C. Castiglioni, *J. Am. Chem. Soc.,* 2009, **131**, 6591.
64 A. Troisi, *Chem. Soc. Rev.,* 2011, **40**, 2347.
65 O. D. Jurchescu, J. Baas and T. T. M. Palstra, *Appl. Phys. Lett.*, 2004, **84**, 3061.
66 M. Yamagishi, J. Takeya, Y. Tominari, Y. Nakazawa, T. Kuroda, S. Ikehata, M. Uno, T. Nishikawa and T. Kawase, *Appl. Phys. Lett.*, 2007, **90**, 182117.
67 V. Podzorov, E. Menard, A. Borissov, V. Kiryukhin, J. A. Rogers and M. E. Gershenson, *Phys. Rev. Lett.*, 2004, **93**, 086602.
68 V. C. Sundar, J. Zaumseil, V. Podzorov, E. Menard, R. L. Willett, T. Someya, M. E. Gershenson and J. A. Rogers, *Science*, 2004, **303**, 1644.
69 A. P. Micolich, L. L. Bell and A. R. Hamilton, *J. Appl. Phys.*, 2007, **102**, 084511.
70 T. Takenobu, T. Takahashi, J. Takeya, Y. Iwasa, *Appl. Phys. Lett.*, 2007, **90**, 013507.
71 T. Uemura, Y. Hirose, M. Uno, K. Takimiya and J. Takeya, *Appl. Phys. Express*, 2009, **2**, 111501.
72 H. Minemawari, T. Yamada, H. Matsui, J. Tsutsumi, S. Haas, R. Chiba, R. Kumai and T. Hasegawa, *Nature*, 2011, **475**, 364.
73 H. Li, B. C-K. Tee, J. J. Cha, Y. Cui, J. W. Chung, S. Y. Lee and Z. Bao, *J. Am. Chem. Soc.*, 2012, **134**, 2760.
74 S. Sato, S. Seki, Y. Honsho, L. Wang, H. Nikawa, G. Luo, J. Lu, M. Haranaka, T. Tsuchiya, S. Nagase and T. Akasaka, *J. Am. Chem. Soc.*, 2011, **133**, 2766.
75 S. Sato, H. Nikawa, S. Seki, L. Wang, G. Luo, J. Lu, M. Haranaka, T. Tsuchiya, S. Nagase, and T. Akasaka, *Angew. Chem. Int. Ed.*, 2012, **51**, 1589.
76 S. Sato, S. Seki, Y. Honsho, L. Wang, H. Nikawa, G. Luo, J. Lu, M. Haranaka, T. Tsuchiya, S. Nagase, T. Akasaka, *J. Am. Chem. Soc.*, 2011, **133**, 2766.
77 A. Saeki, S. Seki, T. Takenobu, Y. Iwasa and S. Tagawa, *Adv. Mater.*, 2008, **20**, 920.
78 J. Takeya, J. Kato, K. Hara, M. Yamagishi, R. Hirahara, K. Yamada, Y. Nakazawa, S. Ikehata, K. Tsukagoshi, Y. Aoyagi, T. Takenobu and Y. Iwasa, *Phys. Rev. Lett.*, 2007, **98**, 196804.
79 C. Reese and Z. Bao, *Adv. Mater.*, 2007, **19**, 4535.
80 T. Amaya, S. Seki, T. Moriuchi, K. Nakamoto, T. Nakata, H. Sakane, A. Saeki, S. Tagawa and T. Hirao, *J. Am. Chem. Soc.*, 2009, **131**, 408.
81 Y. Yamamoto, T. Fukushima, W. Jin, A. Kosaka, T. Hara, T. Nakamura, A. Saeki, S. Seki, S. Tagawa and T. Aida, *Adv. Mater.*, 2006, **18**, 1297.
82 A. Saeki, S. Seki, Y. Shimizu, T. Yamao and S. Hotta, *J. Chem. Phys.*, 2010, **132**, 134509.
83 T. C. Narayan, T. Miyakai, S. Seki and M. Dincă, *J. Am. Chem. Soc.*, 2012, **134**, 12932.
84 L. Sun, T. Miyakai, S. Seki and M. Dinca, *J. Am. Chem. Soc.*, 2013, **135**, 8185.
85 E. Kayahara, T. Iwamoto, H. Takaya, T. Suzuki, M. Fujitsuka, T. Majima, N. Yasuda, N. Matsuyama, S. Seki and S. Yamago, *Nature Commun.*, 2013, **4**, 2694.
86 A. Fukazawa, D. Kishi, Y. Tanaka, S. Seki and S. Yamaguchi, *Angew. Chem. Int. Ed.*, 2013, **52**, 12091.
87 B. M. Schmidt, S. Seki, B. Topolinski, K. Ohkubo, S. Fukuzumi, H. Sakurai, and D. Lentz, *Angew. Chem. Int. Ed.*, 2012, **51**, 11385.
88 M. Pfannmöller, W. Kowalsky and R. R. Schröder, *Energy Environ. Sci.*, 2013, **6**, 2871.
89 T. M. Clarke and J. R. Durrant, *Chem. Rev.*, 2010, **110**, 6736.
90 A. P. H. J. Schenning and E. W. Meijer, *Chem. Commun.*, 2005, 3245.
91 P. Pramod, K. George Thomas and M. V. George, *Chem. Asian J.*, 2009, **4**, 806
92 S. H. Kim and J. R. Parquette, *Nanoscale*, 2012, **4**, 6940.
93 T. Aida, E. W. Meijer and S. Stupp, *Science*, 2012, **335**, 813.
94 F. S. Schoonbeek, J. H. Van Esch, B. Wegewijs, D. B. A. Rep, M. P. de Haas, T. M. Klapwijk, R. M. Kellogg and B. L. Feringa, *Angew. Chem. Int. Ed.,* 1999, **38**, 1393.
95 D. J. Abdallah and R. G. Weiss, *Adv. Mater.,* 2000, **12**, 1237.
96 A. Ajayaghosh and S. J. George, *J. Am. Chem. Soc.*, 2001, **123**, 5148.
97 A. R. Hirst, B. Escuder, J. F. Miravet and D. K. Smith, *Angew. Chem. Int. Ed.*, 2008, **47**, 8002.
98 S. S. Babu, S. Prasanthkumar and A. Ajayaghosh, *Angew. Chem. Int. Ed.*, 2012, **51**, 1766.
99 S. S. Babu, V. K. Praveen and A. Ajayaghosh, *Chem. Rev.*, 2014, **114**, 1973.
100 S. Prasanthkumar, A. Saeki, S. Seki and A. Ajayaghosh, *J. Am. Chem. Soc.,* 2010, **132**, 8866.
101 S. Prasanthkumar, A. Gopal and A. Ajayaghosh, *J. Am. Chem. Soc.,* 2010, **132**, 13206.
102 Z. Chen, A. Lohr, C. R. Saha-Möller and F. Würthner, *Chem. Soc. Rev.*, 2009, **38**, 564.
103 F. Würthner, T. E. Kaiser and C. R. Saha-Möller, *Angew. Chem. Int. Ed.*, 2011, **50**, 3376.
104 T. Seki, X. Lin and S. Yagai, *Asian J. Org. Chem.*, 2013, **2**, 708.
105 S. Yagai, M. Usui, T. Seki, H. Murayama, Y. Kikkawa, S. Uemura, T. Karatsu, A. Kitamura, A. Asano and S. Seki, *J. Am. Chem. Soc.*, 2012, **134**, 7983.
106 W.-S. Li, A. Saeki, Y. Yamamoto, T. Fukushima, S. Seki, N. Ishii, K. Kato, M. Takata and T. Aida, *Chem. Asian J.*, 2010, **5**, 1566.
107 C. Didraga, A. Pugžlys, P. R. Hania, H. von Berlepsch, K. Duppen and J. Knoester, *J. Phys. Chem. B*, 2004, **108**, 14976.
108 D. M. Eisele, J. Knoester, S. Kirstein, J. P. Rabe and D. A. Vanden Bout, *Nat. Nanotech.*, 2009, **4**, 658.
109 H. Shao, J. Seifert, N. C. Romano, M. Gao, J. J. Helmus, C. P. Jaroniec, D. A. Modarelli and J. R. Parquette, *Angew. Chem. Int. Ed.*, 2010, **49**, 7688.
110 S. Sengupta, D. Ebeling, S. Patwardhan, X. Zhang, H. von Berlepsch, C. Böttcher, V. Stepanenko, S. Uemura, C. Hentschel, H. Fuchs, F. C. Grozema, L. D. A. Siebbeles, A. R. Holzwarth, L. Chi and F. Würthner, *Angew. Chem. Int. Ed.*, 2012, **51**, 6378.

111 Y. Yamamoto, T. Fukushima, Y. Suna, N. Ishii, A. Saeki, S. Seki, S. Tagawa, M. Taniguchi, T. Kawai and T Aida, *Science*, 2006, **314**, 1761.
112 Y. Yamamoto, T. Fukushima, A. Saeki, S. Seki, S. Tagawa, N. Ishii and T. Aida, *J. Am. Chem. Soc.* 2007, **129**, 9276.
113 M. J. Frampton and H. L. Anderson, *Angew. Chem. Int. Ed.*, 2007, **46**, 1028.
114 A. Harada, A. Hashidzume, H. Yamaguchi and Y. Takashima, *Chem. Rev.*, 2009, **109**, 5974.
115 S. Brovelli and F. Cacialli, *Small*, 2010, **6**, 2796.
116 K. Sugiyasu, Y. Honsho, R. M. Harrison, A. Sato, T. Yasuda, S. Seki and M. Takeuchi, *J. Am. Chem. Soc.*, 2010, **132**, 14754.
117 Y. Ouchi, K. Sugiyasu, S. Ogi, A. Sato and M. Takeuchi, *Chem. Asian J.*, 2012, **7**, 75.
118 R. Shomura, K. Sugiyasu, T. Yasuda, A. Sato and M. Takeuchi, *Macromolecules*, 2012, **45**, 3759.
119 J. Terao, Y. Tanaka, S. Tsuda, N. Kambe, M. Taniguchi, T. Kawai, A. Saeki and S. Seki, *J. Am. Chem. Soc.*, 2009, **131**, 18046.
120 J. Terao, *Polym. Chem.*, 2011, **2**, 2444.
121 J. Terao, *Chem. Record*, 2011, **11**, 269.
122 J. Terao, A. Wadahama, A. Matono, T. Tada, S. Watanabe, S. Seki, T. Fujihara and Y. Tsuji, *Nat. Commun.*, 2013, **4**, 1691.
123 S. Laschat, A. Baro, N. Steinke, F. Giesselmann, C. Haegele, G. Scalia, R. Judele, E. Kapatsina, S. Sauer, A. Schreivogel and M. Tosoni, *Angew. Chem. Int. Ed.*, 2007, **46**, 4832.
124 S. Sergeyev, W. Pisula and Y. H. Geerts, *Chem. Soc. Rev.,* 2007, **36**, 1902.
125 E.-K. Fleischmann and R. Zentel, *Angew. Chem. Int. Ed.*, 2013, **52**, 8810.
126 M. Funahashi and J. Hanna, *Phys. Rev. Lett.*, 1997, **78**, 2184.
127 Z. An, J. Yu, S. C. Jones, S. Barlow, S. Yoo, B. Domercq, P. Prins, L. D. A. Siebbeles, B. Kippelen and S. R. Marder, *Adv. Mater.*, 2005, **17**, 2580.
128 Y. Shimizu, K. Oikawa, K. Nakayama and D. Guillon, *J. Mater. Chem.*, 2007, **17**, 4223.
129 P. G. Schouten, J. M. Warman, M. P. de Haas, M. A. Fox and H.-L. Pan, *Nature*, 1991, **353**, 736.
130 D. Adam, P. Schuhmacher, J. Simmerer, L. Häussling, K. Siemensmeyer, K. H. Etzbach, H. Ringsdorf and D. Haarer, *Nature,* 1994, **371**, 141.
131 J. M. Warman and A. M. Van de Craats, *Mol. Cryst. Liq. Cryst.*, 2003, **396**, 41.
132 J. Piris, M. G. Debije, N. Stutzmann, B. W. Laursen, W. Pisula, M. D. Watson, T. Bjørnholm, K. Müllen and J. M. Warman, *Adv. Funct. Mater.*, 2004, **14**, 1053.
133 J. Motoyanagi, Y. Yamamoto, A. Saeki, M. A. Alam, A. Kimoto, A. Kosaka, T. Fukushima, S. Seki, S. Tagawa and T. Aida, *Chem. Asian J.*, 2009, **4**, 876.
134 W.-S. Li, Y. Yamamoto, T. Fukushima, A. Saeki, S. Seki, S. Tagawa, H. Masunaga, S. Sasaki, M. Takata and T. Aida, *J. Am. Chem. Soc.*, 2008, **130**, 8886.
135 Q. Xiao, T. Sakurai, T. Fukino, K. Akaike, Y. Honsho, A. Saeki, S. Seki, K. Kato, M. Takata and T. Aida, *J. Am. Chem. Soc.*, 2013, **135**, 18268.
136 T. Sakurai, K. Shi, H. Sato, K. Tashiro, A. Osuka, A. Saeki, S. Seki, S. Tagawa, S. Sasaki, H. Masunaga, K. Osaka, M. Takata and T. Aida, *J. Am. Chem. Soc.*, 2008, **130**, 13812.
137 T. Sakurai, K. Tashiro, Y. Honsho, A. Saeki, S. Seki, A. Osuka, A. Muranaka, M. Uchiyama, J. Kim, S. Ha, K. Kato, M. Takata and T. Aida, *J. Am. Chem. Soc.*, 2011, **133**, 6537.
138 S. Tanaka, T. Sakurai, Y. Honsho, A. Saeki, S. Seki, K. Kato, M. Takata, A. Osuka and T. Aida, *Chem. Eur. J.*, 2012, **18**, 10554.
139 V. Lemaur, D. A. Da Silva Filho, V. Coropceanu, M. Lehmann, Y. Geerts, J. Piris, M. Debije, A. Van de Craats, K. Senthilkumar, L. Siebbeles, J. Warman, J.-L. Brédas, J. Cornil, *J. Am. Chem. Soc.*, 2004, **126**, 3271.
140 V. Marcon, D. Breib., W. Pisula, W. Dahl, J. Kirkpatrick, S. Patwardhan, F. Grozema, D. Andrienko, *J. Am. Chem. Soc.*, 2009, **131**, 11426.
141 T. Osawa, T. Kajitani, D. Hashizume, H. Ohsumi, S. Sasaki, M. Takata, Y. Koizumi, A. Saeki, S. Seki, T. Fukushima and T. Aida, *Angew. Chem. Int. Ed.*, 2012, **51**, 7990.
142 M.-C. Yeh, Y.-L. Su, M.-C. Tzeng, C. W. Ong, T. Kajitani, H. Enozawa, M. Takata, Y. Koizumi, A. Saeki, S. Seki and T. Fukushima, *Angew. Chem. Int. Ed.*, 2012, **51**, 7990.
143 B. Dong and H. Maeda, *Chem. Commun.*, 2013, **49**, 4085.
144 H. Maeda, *Bull. Chem. Soc. Jpn.*, 2013, **86**, 1359.
145 Y. Haketa, S. Sasaki, N. Ohta, H. Masunaga, H. Ogawa, N. Mizuno, F. Araoka, H. Takezoe and H. Maeda, *Angew. Chem. Int. Ed.*, 2010, **49**, 10079.
146 B. Dong, T. Sakurai, Y. Bando, S. Seki, K. Takaishi, M. Uchiyama, A. Muranaka and H. Maeda, *J. Am. Chem. Soc.*, 2013, **135**, 14797.
147 B. Dong, T. Sakurai, Y. Honsho, S. Seki, and H. Maeda, *J. Am. Chem. Soc.*, 2013, **135**, 1284.
148 A. Saeki, T. Fukumatsu and S. Seki, *Macromolecules*, 2011, **44**, 3416.
149 Y. Yasutani, A. Saeki, T. Fukumatsu, Y. Koizumi and S. Seki, *Chem. Lett.* 2013, **42**, 19.
150 C. Coulon and R. Clérac, *Chem. Rev*., 2004, **104**, 5655.
151 G. Feher, R. C. Fletcher and E. A. Gere, *Phys. Rev*., 1955, **100**, 1784.
152 G. Feher, *Phys. Rev*., 1959, **114**, 1219.
153 M. Nechtschein, F. Devreux, F. Genoud, M. Guglielmi and K. Holczer, *Phys. Rev. B*, 1983, **27**, 61.
154 J. C. Scott, P. Pfluger, M. T. Krounbi and G. B. Street, *Phys. Chem. B*, 1983, **28**, 2140.
155 K. Tanaka, T. Shichiri, K. Yoshizawa, T. Yamabe, S. Hotta, W. Shimotsuka and Y. Deguchi, *Solid State Commun*., 1984, **51**, 565.
156 K. Tanaka, K. Yoshizawa, T. Koike, T. Yamabe, J. Yamauchi, Y. Deguchi and S. Yata, *Solid State Commun*., 1984, **52**, 343.
157 K. Marumoto, T. Sakamoto, S. Watanabe, H. Ito and S. Kuroda, *Jpn. J. Appl. Phys.,* 2007, **46**, L1191.
158 K. Marumoto, N. Arai, H. Goto, M. Kijima, K. Murakami, Y. Tominari, J. Takeya, Y. Shimoi, H. Tanaka, S. Kuroda, T. Kaji, T. Nishikawa, T. Takenobu and Y. Iwasa, *Phys. Rev. B*, 2011, **83**, 075302.
159 H. Matsui, T. Hasegawa and Y Tokura, *Phys, Rev. Lett*., 2008, **100**, 126601.
160 H. Matsui, A. S. Mishchenko and T. Hasegawa, *Phys, Rev. Lett*., 2010, **104**, 056602.

161 H. Matsui, D. Kumaki, E. Takahashi, K. Takimiya, S. Tokito and T. Hasegawa, *Phys, Rev. B*, 2012, **85**, 035308.
162 R. Kubo and K. Tomita, *J. Phys. Soc. Jpn*., 1954, **9**, 888.
163 A. S. Mishchenko, S. Mishchenko, N. Nagaosa, A. Alvermann, H. Fehske, G. De Filippis, V. Cataudella and O. P. Sushkov, *Phys, Rev. B*, 2009, **79**, 180301.
164 D. S. Weiss and M. Abkowitz, Chem. *Rev*, 2010, **110**, 479.
165 N. S. Sariciftci, L. Smilowits, A. J. Heeger and F. Wudl, *Science*, 1992, **258**, 1474.
166 V. Dyakonov, G. Zoriniants, M. Scharber, C. J. Brabec, R. A. J. Janssen, J. C. Hummelen and N. S. Sariciftci, *Phys. Rev. B*, 1999, **59**, 8019.
167 K. Furukawa, Y. Sugishima, H. Fujiwara and T. Nakamura, *Chem. Lett*, 2011, **40**, 292.
168 S. Jin, X. Ding, X. Feng, M. Supur, K. Furukawa, S. Takahashi, M. Addicoat, M. E. El-Khouly, T. Nakamura, S. Irle, S. Fukuzumi, A. Nagai and D. Jiang, *Angew. Chem. Int. Ed.,* 2013, **52**, 2017.
169 X. Feng, L. Chen, Y. Honsho, O. Saengsawang, L.Liu, L. Wang, A. Saeki, S. Irle, S. Seki, Y. P. Dong and D. Jiang, *Adv. Mater.*, 2012, **24**, 3026.
170 L. Chen, Y. Honsho, S. Seki, and D. Jiang, *J. Am. Chem. Soc.*, 2010, **132**, 6742.
171 J. Guo, Y. Xu, S. Jin, L. Chen, T. Kaji, Y. Honsho, M. A. Addicoat, J. Kim, A. Saeki, H. Ihee, S. Seki, S. Irle, M. Hiramoto, J. Gao and D. Jiang, *Nat. Commun.*, 2013, **4**, 2736.
172 T. Fukumatsu A. Saeki and S. Seki, *J. Photopolym. Sci. Technol*., 2012, **25**, 665.
173 K. Higashiguchi, K. Yamamoto and K. Matsuda, *Org. Lett.,* 2010, **12**, 5284.
174 M. Shinomiya, K. Higashiguchi and K. Matsuda, *J. Org. Chem.,* 2013, **78**, 9282.
175 B. Schlicke, P. Belser, L. De Cola, E. Sabbioni and V. Balzani, *J. Am. Chem. Soc.,* 1999, **121**, 4207.
176 E. A. Weiss, M. J. Ahrens, L. E. Sinks, A. V. Gusev, M. A. Ratner and M. R. Wasielewski, *J. Am. Chem. Soc.,* 2004, **126**, 5577.
177 W. Wang, S. Wang, X. Li, J.-P. Collin, J. Liu, P. N. Liu and N. Lin, *J. Am. Chem. Soc.,* 2010, **132**, 8774.
178 S. Nishizawa, J. Hasegawa and K. Matsuda, *Chem. Phys. Lett.,* 2013, **132**, 187.
179 Q. Lu, K. Liu, H. Zhang, Z. Du, X. Wang and F. Wang, *ACS Nano*, 2009, **3**. 3861.
180 V. Kaliginedi, P. Moreno-García, H. Valkenier, W. Hong, V. M. García-Suárez, P. Buiter, J. L. H. Otten, J. C. Hummelen, C. J. Lambert and T. Wandlowski, *J. Am. Chem. Soc.*, 2012, **134**, 5262.
181 W. Hong, H. Li, S.-X. Liu, Y. Fu, J. Li, V. Kaliginedi, S. Decurtins and T. Wandlowski, *J. Am. Chem. Soc.,* 2012, **134**, 19425.
182 J. K. Tomfohr and O. F. Sankey, *Phys. Status Solidi B*, 2002, **233**, 59.
183 H. Liu, N. Wang, J. Zhao, Y. Guo, X. Yin, F. Y. C. Boey and H. Zhang, *ChemPhysChem*, 2008, **9**, 1416.